Creep Deformation and Long-Term Strength of Ice-Rich Permafrost in Northern Alaska

Ziyi Wang*[1]; Ming Xiao[1]; Matthew Bray[2]; Dmitry Nicolsky[3]; Xiaohang Ji[1]

[1]Department of Civil and Environmental Engineering, The Pennsylvania State University, University Park, PA 16802, United States of America.

[2]Institute of Northern Engineering, University of Alaska Fairbanks, Fairbanks, AK 99775-5900, United States of America.

[3]Geophysical Institute, University of Alaska Fairbanks, Fairbanks, AK 99775, United States of America.

November 19, 2024

This manuscript is a non-peer reviewed preprint submitted to EarthArXiv.

This manuscript has been submitted to the Journal of Geotechnical and Geoenvironmental Engineering for publication consideration. Future versions may contain different content.

*E-mail: ziyiwang@psu.edu (Corresponding author)

Creep Deformation and Long-Term Strength of Ice-Rich Permafrost in Northern Alaska

Ziyi Wang, S.M.ASCE[1]; Ming Xiao, Ph.D., P.E., F.ASCE[2]; Matthew Bray, Ph.D.[3]; Dmitry Nicolsky, Ph.D.[4]; Xiaohang Ji, S.M.ASCE[5]

[1]Ph.D. Candidate, Department of Civil and Environmental Engineering, The Pennsylvania State University, University Park, PA 16802, United States of America. Email: ziyiwang@psu.edu (Corresponding author)

[2]Professor, Department of Civil and Environmental Engineering, The Pennsylvania State University, University Park, PA 16802, United States of America. Email: mzx102@psu.edu.

[3]Research Professional, Institute of Northern Engineering, University of Alaska Fairbanks, Fairbanks, AK 99775-5900, United States of America. Email: mtbray@alaska.edu.

[4]Research Associate Professor, Geophysical Institute, University of Alaska Fairbanks, Fairbanks, AK 99775, United States of America. Email: djnicolsky@alaska.edu.

[5]Ph.D. Candidate, Department of Civil and Environmental Engineering, The Pennsylvania State University, University Park, PA 16802, United States of America. Email: xhji@psu.edu.

Abstract: The degradation of permafrost alters deformation and long-term strength, posing challenges to existing and future civil infrastructure in northern Alaska. Long-term strength is a critical parameter in the design of civil projects; yet data on the creep deformation and long-term strength of undisturbed permafrost in northern Alaska remain limited. Soil particle fraction, unfrozen water content, temperature, and salinity may interactively affect creep deformation and long-term strength of permafrost; however, their interactive effects are not well understood. In this study, field samples of relatively undisturbed permafrost from the upper 1.5 meters of the Arctic Coastal Plain near Utqiaġvik, Alaska were first retrieved and analyzed. The permafrost was characterized as saline ice-rich silty sand and non-uniformly distributed ice. We conducted constant stress creep tests, unconfined compression strength tests, and unfrozen water content tests to assess the mechanical and physical properties of the permafrost cores. The results indicated that the long-term strength of the permafrost decreased by nearly 90% from -10℃ to -2℃. At -10℃, the long-term strength increased by approximately 120% as the soil particle fraction rose from 0.14 to 0.26. The strengthening effect of soil particles diminished at higher temperatures and higher salinity due to the influence of unfrozen water. A quantitative tool has been developed to predict the long-term strength of ice-rich permafrost, incorporating the effects of soil particle fraction and temperature. The findings of this study can potentially support infrastructure design and planning in northern Alaska in the context of global climate change.

Keywords: permafrost, creep, long-term strength, soil particle fraction, temperature, unfrozen water, salinity

Introduction

Permafrost is soil or rock that remains at or below 0℃ for at least two consecutive years. It is widely distributed in high-latitude regions and occupies 24% of the land area of the northern hemisphere (Anisimov and Nelson 1996). In Arctic regions, permafrost has historically provided a reliable foundation for civil infrastructure, with structures anchored into permafrost to withstand various loads (Nixon and McRoberts 1976; Morgenstern et al. 1980; Hjort et al. 2022). Permafrost, as a visco-plastic material, typically exhibits three phases of time-dependent deformation: primary, secondary, and tertiary creep. Creep strength of permafrost is therefore time-dependent and long-term strength can be defined by the stress above which non-attenuating creep occurs (Tsytovich 1975). The design of civil infrastructure foundations in cold regions aims to ensure that applied stress does not exceed the long-term strength of permafrost over the structure's lifespan (Vyalov et al. 1969; Ladanyi and Johnston 1974). Global climate change, however, is driving the warming of the Arctic at up to four times the rate of lower latitudes (Rantanen et al. 2022). As air temperatures in the Arctic increase over time, ground temperatures rise, driving near-surface permafrost degradation (Biskaborn et al. 2019; Wang et al. 2023a, b). The degradation of permafrost alters the physical and mechanical properties, which in turn adversely affects the creep deformation and long-term strength of permafrost. The weakened mechanical properties of permafrost pose threats to civil infrastructures. In northern Alaska, permafrost degradation is estimated to damage 59% of public infrastructure by the end of this century (Creel et al. 2024). Understanding creep behavior and long-term strength of permafrost is critical to support civil infrastructure planning and design.

The deformation and strength of frozen soils has been extensively investigated for the last several decades (e.g., Vialov 1959; Ladanyi 1972; Sayles 1974a, b; Hooke et al. 1980; Weaver and Morgenstern 1981; Zhu and Carbee 1984; Vyalov 1986; Orth 1988; Shelman et al. 2014; Yang et al. 2015; Shastri et al. 2021; Wang et al. 2022; Schindler et al. 2024). Secondary creep rate is of particular interest in engineering considerations, as it dominates in ice-rich permafrost under moderate stress conditions and provides an estimate of long-term strength (Vyalov 1969; Thompson and Sayles 1972). The primary factors influencing secondary creep rate include the volumetric fraction of soil particle or ice (Goughnour and Andersland 1968; Arenson et al. 2004), temperature (Sayles 1968), solute concentration (Nixon and Lem 1984), and the state of stress (Zhu and Carbee 1987; Arenson and Springman 2005b; Cudmani et al. 2022).

Goughnour and Andersland (1968) conducted one of the earliest laboratory studies on the effect of volumetric sand fraction on the strength of frozen soil. They observed that the compressive strength of frozen soil increased slightly with volumetric sand fraction up to 42%. Beyond 42%, a further increase in sand fraction led to a rapid increase in strength due to the influence of interparticle friction. Subsequent experimental results reported by Baker and Konrad (1985) align with the finding of Goughnour and Andersland (1968). Baker (1979) extended the range of sand fraction and found that maximum strength is typically achieved when the soil is ice-saturated and pores are filled with ice. Beyond this peak, the strength of frozen soil declines sharply as sand fraction increases further and the ice fraction approaches zero (Andersland and Ladanyi, 2003). Based on a synthesis of experimental data, Ting et al. (1984) proposed mechanism maps to describe the behavior of frozen soil. They concluded that increasing the sand volume fraction from

0% to 60% enhanced the compressive strength at -7.6°C and reduced the secondary creep rate at -15.4°C.

Frozen soil with very low soil particle fractions can behave differently near the melting temperature. For example, Hooke et al. (1972) observed that a sample with 2.1% volumetric sand fraction had a creep rate 40% higher than that of pure ice. Arenson and Springman (2005b) observed that, near the melting temperature, adding 5% to 15% soil particles by volume to ice reduced shear strength and increased the secondary creep rate. These observations of weakened frozen soil compared to ice at higher temperatures are often attributed to the increased unfrozen water content in soil-ice systems (Duval 1977). Unfrozen water reduces the creep resistance of permafrost by weakening the ice matrix, facilitating the relative particle displacement, and modulating stress distributions at particle-particle and particle-ice contacts (Moore 2014). Unfrozen water content depends on how close the temperature is to the melting point. Additionally, solutes can lower the melting point of ice and further influence the amount of unfrozen water. Salinity can be therefore used to study the effects of unfrozen water. Nixon and Lem (1984) and Hivon and Sego (1995) quantified the weakening effect of salinity on the creep rate and compressive strength of frozen soil through a series of laboratory tests. Moore (2014) highlighted the competition between the strengthening effect of soil particles in enhancing creep resistance and the weakening effects of unfrozen water at particle-ice interfaces.

Ice-rich saline permafrost is prevalent in the coastal regions of northern Alaska with annual ground temperatures varying by depth from approximately -10°C to the melting point (Wang et al. 2024a, b; Tourei et al. 2024). Understanding the creep deformation and long-term strength of relatively undisturbed permafrost under varying soil conditions—volumetric soil particle fraction, unfrozen water content, temperature, and salinity—is essential for designing climate-resilient infrastructure. However, the dataset on creep and long-term strength of undisturbed permafrost in northern Alaska remains limited. The interactive effects of soil particle fraction, unfrozen water content, temperature, and salinity on the deformation and long-term strength of permafrost are still not fully understood. For example, no quantitative study has demonstrated how temperature alters the influence of soil particle fraction on creep and long-term strength of ice-rich permafrost. This knowledge gap hinders the development of quantitative tools to describe permafrost creep and long-term strength for infrastructure risk assessments at local and regional scales.

This paper presents field sampling of ice-rich permafrost on the tundra near Utqiaġvik, Alaska and laboratory tests on the retrieved permafrost samples. This study aims to (1) characterize geophysical and geomechanical properties of permafrost in the coastal regions of northern Alaska to add to the scarce database, (2) investigate the interactive effects of soil particle fraction, unfrozen water content, temperature, and salinity on creep deformation and long-term strength of permafrost, and (3) develop a quantitative tool to describe the creep behavior and long-term strength of permafrost under varying soil conditions.

Field Testing and Geological History

Soil Sampling

The field sampling was conducted at five locations on the undisturbed permafrost tundra near Utqiaġvik, Alaska in August 2022. Figure 1 presents an aerial view of the tundra with the layouts of the five boreholes, labeled S1 (71.3231°N 156.6144°W), S2 (71.3244°N 156.6103°W), S3

(71.3264°N 156.5994°W), S4 (71.3294°N 156.5933°W), and S5 (71.3322°N 156.5842°W). A total of 562.1 cm of relatively undisturbed permafrost cores of 4.0 – 4.3 cm in diameter were obtained using a battery-powered auger. The active layer thickness of the permafrost tundra was 14 to 27.9 cm at the time of the sampling. The vegetated active layer was carefully removed at the borehole locations and set aside. Each permafrost core was wrapped in plastic film with aluminum foil and placed into a portable freezer with frozen gel packs to keep the samples frozen. All collected cores were kept at negative temperatures during the entire period of transportation to the lab. After coring, the vegetated active layer was carefully restored to its original position. The study sites are located within the Barrow quadrangle of the geological map of Alaska (Wilson et al. 2015). This region is primarily covered with Quaternary unconsolidated surficial deposits, consisting mainly of silty sand.

Cryostratigraphy of Deposits

Figure 2 depicts the cryostratigraphy of the primary surficial deposits at the study site. Cryostructure is the pattern of ice inclusions within a frozen soil; it is closely associated with cryolithology and Quaternary depositional environments. Soil types and cryostructure were identified through a combination of field and laboratory characterizations. At location S1 (Figure 2a), the active layer thickness was 14 cm at the time of sampling. From 14 to 90 cm depth, the core was primarily dark brown clayey silt with gravel. Ice occurred occasionally as 1.3-cm thick lenticular ice lenses. From 90 cm to 103 cm, the soil was medium brown silty sand with sparse fine gravel and reticulate ice.

At location S2 (Figure 2b), the active layer thickness was 21.6 cm during sampling. The soil consisted of peat with woody fragments and roots from 21.6 cm to 36.8 cm. Ice was present as thin lenticular lenses and random ice lenses up to 0.1-cm thick. From 36.8 cm to 83.8 cm, the core segments were primarily ice. From 83.8 cm to 147 cm, a general transition was observed from gray ice-rich sand to medium brown and slightly sandy silt with sparse fine gravel intermixed with ice zones. From 152 cm to 170 cm, the soil was brown silty sand with sparse fine gravel and contained only pore ice.

At location S3 (Figure 2c), the active layer thickness was 20.3 cm. The soil was ice-rich and primarily composed of peat and silty sand. The sand was highly silty with sparse fine gravel. From 20.3 cm to 40.6 cm, the soil was peat to silty peat. Ice was present in an organic matrix above 30.5 cm; below 30.5 cm was primarily ice. From 40.6 cm to 66.0 cm, the subsurface was primarily ice. Below the ice layer, the soil was typically silty sand suspended within ice (i.e., ataxitic cryostructure). From 66.0 cm to 104.1 cm, the soil was medium brown silty sand. Below 104.1 cm, the soil was gray silty sand.

At location S4 (Figure 2d), the active layer thickness was 23.8 cm during sampling. Most of the sampled sections were ice-rich. The soil consisted of silty peat to silt from 23.8 cm to 45.7 cm depth, silty sand suspended within ice from 48.3 cm to 142.2 cm depth, and silty sand with fine gravel with decreasing ice content with depth from 132.1 cm.

At location S5 (Figure 2e), the active layer thickness was 27.9 cm. The soil was peat to silty peat from 27.9 cm to 50.8 cm depth with pore ice (above 41.9 cm) and visible vertical and horizontal ice lenses (below 41.9 cm). From 50.8 cm to 64.8 cm, the soil was intermixed peat and medium brown soil. Ice was present in the organic matrix. From 64.8 cm to 104.1 cm, the soil consisted of intermixed peat and medium brown silty sand suspended in ice (i.e., ataxitic cryostructure). Ice and silt layers occurred from 104.1 cm to 140.7 cm. From 140.7 cm to 154.9 cm, the soil was medium brown silt with layered and reticulate ice lenses up to 0.3-cm thick, with several ice lenses up to 2-cm thick.

Materials and Methods

Physical Properties and Sample Preparation

Laboratory tests included unconfined constant stress creep (CSC), unconfined compressive strength (UCS), and unfrozen water content (UWC) tests. We assessed physical properties such as total water content, Atterberg limits, grain size distribution, and salinity using the samples after the mechanical and unfrozen water content tests. Dry density, soil particle fraction, total volumetric water content, and specific gravity were calculated based on phase relationships. In this study, soil particle fraction represents the volumetric fraction of soil particles within frozen soil. These calculations assumed that the samples were fully saturated. Atterberg limit tests were repeatedly conducted for each sample until consistent and reproducible results were obtained (ASTM 2017). The grain size distributions of the samples were determined by conducting sieve analysis and hydrometer analysis, per ASTM C136 and ASTM D422, respectively.

The salinity of the permafrost was determined by measuring the concentration of soluble salts in the soil. The test method followed the standard ISO 11265:1994 (ISO 1994). A Milwaukee MW802 Pro Combo Meter was used for salinity measurements. The samples were first thawed.

Then, a soil-water suspension was prepared by mixing 50 g of dry soil and 250 mL of distilled water. The suspension was soaked for an hour to let the salts dissolve completely. We calibrated the instrument with a standard solution of 1413 μS/cm. The measuring probe was rinsed with distilled water before taking each measurement in the suspension. Three salinity measurements were performed for each sample. The measured conductivity was converted to parts per thousand (ppt), which is approximately equivalent to g/L. Table 1 presents the basic physical properties of the tested samples. The sample number indicates the coring location (S2 to S5) and the sequential number of the sample from the top to the bottom depth in each borehole.

Selected permafrost cores for laboratory testing were uniform in both soil type and cryostructure. We chose samples with a minimum length-to-diameter ratio of 2:1 to reduce end effects on mechanical behavior. Samples with significant tapering and uneven diameters along their length were excluded from testing. The diameter of the selected samples varied between 4.0 to 4.5 cm. Figure 3 consists of photographs of the selected permafrost samples before the mechanical tests. The selected permafrost cores were ice-rich, with soil particles suspended in ice. The soil particle fraction, θ_s, of the samples in the mechanical tests ranged from 14% to 43%. Figure 4 illustrates the grain-size distributions of the selected samples for the laboratory tests. Following the Unified Soil Classification System and Arenson et al. (2007), the tested samples were classified as ice-rich silty sand (SM) based on soil phase classifications and ice content measurements. The comprehensive photographs of the retrieved samples from each borehole are shown in Table S1 in the supplementary materials.

Mechanical Tests – UCS and CSC

We tested six samples for UCS and six samples for multi-stage CSC with stepped increase in stress; three samples were tested at -2℃ and three at -10℃ for both UCS and CSC testing. Figure 5 illustrates the test setup for these tests. The UCS tests were performed on electro-mechanical screw-driven load frames, at a strain rate of 0.6 per hour according to ASTM D7300. The loading frames were placed in a walk-in cold room maintained at room temperature of -5℃. Insulated chambers surrounded the loading pistons and frame. Within each chamber, a convection-driven heat exchanger was placed in series with an external cold bath to achieve a specific temperature and maintain chamber temperature precision within ± 0.03℃. The air temperature around the samples was monitored by four calibrated thermistors in close proximity to the sample. Figures S1 and S2 in the supplementary materials show the temperature variation during each test. A latex membrane was placed around each sample to eliminate sublimation.

The CSC tests were conducted using an environmentally-equipped servo-control hydraulic load frame. Sample temperature was controlled by fitting a secondary insulated chamber within the main environmental chamber. The secondary chamber contained a convection-driven heat exchanger connected to an external refrigerated recirculating bath with temperature stability of 0.01℃. This temperature-control system maintained chamber temperature precision within ± 0.02℃. We monitored the sample temperature with four calibrated thermistors spaced around the sample. The average of these four temperatures were used as the temperature of the sample. A latex membrane was placed around each sample to eliminate sublimation. Prior to testing, all samples were given a minimum of 24 hours to equilibrate to a constant temperature.

During the CSC tests, the applied load was monitored and maintained within 4.5 N of the target load. Considering the increase in the sample's cross-sectional area due to deformation, which was assumed to be entirely plastic, the load was adjusted during the test to sustain a constant stress condition. This adjustment was made for every 0.13 cm of vertical deformation. After the UCS and CSC tests, we photographed each sample and measured its total water contents. In the CSC tests, a minimum of four increasing stress steps were applied. Each stress level was typically maintained for four days unless tertiary creep occurred. During the CSC tests at -2℃, we applied four stress steps to three samples, with the deviatoric stresses set at 103.4, 172.4 (increased to 206.8 for S4-2), 275.8, and 344.7 kPa. For the CSC tests at -10℃, additional stress steps were conducted on sample S4-2 for a detailed creep analysis, with applied stresses of 172.4, 275.8, 413.7, 586.1, 792.9, 1103.2, and 1379.0 kPa. Based on creep response of S4-2, the stress steps were reduced to four for samples S4-3 and S4-5, with stresses of 586.1, 792.9, 1103.2, and 1379.0 kPa; however, only the first three steps were completed for S4-3 due to temperature control issues.

Unfrozen Water Content (UWC) Tests

The UWC as a function of temperature for 12 samples was measured using a pulsed nuclear magnetic resonance (P-NMR) testing system. The P-NMR testing system included a modified refrigerator for the testing environment. The P-NMR device, complete with a variable temperature probe, was placed inside the refrigerator within an insulated box to maintain the operating temperature of the magnet. Together with external refrigerated circulating baths, this setup precisely controlled the sample temperature. The samples for UWC measurements were cored with a 1.4-cm diameter hole saw, typically to a length of 4 cm. Then, the UWC was measured at -20, -10, -5, -3, -2, -1, -0.5, 5, and 10℃. After each change in temperature, samples were allowed to reach thermal equilibrium for 2 hours. We generally followed the normalization method (Kruse et al. 2018); however, when calculating the UWC, only the value of the free induction decay signal intensity determined at 10℃ was used for the normalization reference value per soil type. The testing method had an accuracy of ± 2% gravimetric water content.

Results and Analyses

Time-dependent Deformation Behavior under the CSC Tests

Figure 6 depicts the creep behavior from the six multi-stage CSC tests. Figures 6a and 6b plot the axial strain and axial strain rate over time at -2℃; Figures 6c and 6d illustrate the progression of axial strain and axial strain rate over time at -10℃. The typical creep behavior of frozen soil is observed: axial strain increases over time, and the strain rate initially decreases (in primary creep), reaches a minimum (in secondary creep), and then increases (in tertiary creep). The stress increase resulted in a jump in the strain rate. At low deviatoric stress levels, permafrost may remain in primary creep by the end of the loading stage, as indicated by not reaching a minimum or constant strain rate. The six permafrost samples all entered a tertiary creep within the tested stress range.

The samples exhibited lower axial strain rates at -10℃ compared to those at -2℃ under the same applied stresses. Specifically, sample S4-2 showed damped creep at -10℃ under 275.8 kPa, unlike the secondary creep or tertiary creep observed at -2℃. Damped creep is characterized by a continuously decreasing strain rate that eventually approaches zero. Moreover, the total axial strain during primary creep at -10℃ was significantly lower than that at -2℃ under the same deviatoric stress. Tertiary creep initiated at much higher stresses within the same testing period for the samples at -10℃ compared to those at -2℃. However, upon reaching a certain stress, the strain rate rapidly increased, leading to eventual failure.

The high recording frequency, low strain rate, and the resolution of the deformation transducer caused the strain rate to oscillate around the mean value (Arenson and Springman 2005a). Figure 7 illustrates the determination of minimum strain rate. Three scenarios were encountered in the determination of minimum strain rate. In the first scenario, a well-defined minimum strain rate was observed followed by an increase in the strain rate, as seen in S4-3 at the third stress stage and S4-2 at the sixth stress stage. In the second scenario, the strain rate stabilized at a constant value, as observed in S4-4 at the third stress stage. In the third scenario, the minimum strain rate may not have been reached, as demonstrated by S4-3 at the first stress stage. For the first scenario, the minimum strain rate was identified at the minimum point. For the latter two scenarios, the minimum strain rate was determined using a moving average of the strain rate over the final 12 hours (Arenson and Springman 2005a), as shown in Eq. (1).

$$\dot{\epsilon}_{avg} = \frac{1}{N}\sum_{i=1}^{N}\dot{\epsilon}_{1,i} \tag{1}$$

where $\dot{\epsilon}_{avg}$ represents the moving average of the strain rate, N denotes the number of measurements within the time window, and $\dot{\epsilon}_1$ is the axial strain rate. In the third scenario, the determined minimum strain rate is considered as an acceptable upper bound for interpreting the stress-strain rate relationship (Arenson and Springman, 2005a; Bray 2012).

In the laboratory, the minimum creep rate of ice and ice-rich frozen soil can be characterized using Glen's flow law (Glen 1955). This power law equation is expressed as:

$$\dot{\epsilon_m} = A\sigma_1^n \tag{2}$$

where $\dot{\epsilon}_m$ is the minimum strain rate, σ_1 is the axial stress, *A* is the fluidity parameter inversely related to the viscosity, and *n* is the stress exponent. Based on the results in Figure 6, the minimum strain rates at each stress stage were plotted in Figure 8. Using Glen's flow law, we determined the secondary creep parameters, *A* and *n*, by correlating axial stress (the applied deviatoric stress in each step of the CSC tests) with the minimum strain rate.

At -2℃, sample S4-4 with the lowest soil particle fraction (0.18) among the three samples exhibited the highest minimum strain rate during the secondary creep compared to the others; sample S4-3 with the highest soil particle fraction (0.27) showed the lowest minimum strain rate. At -10℃, analogously, sample S4-2 with the highest soil particle fraction (0.26) exhibited the lowest minimum strain rate among the three samples. This observation aligns with the synthesis by Ting (1984) indicating that an increase in soil particle fraction enhances the resistance of frozen soil to creep.

Table 2 provides a summary of the minimum strain rate, failure strain, parameters *A*, *n*, and R^2 for the six permafrost samples. The creep parameters show strong correlations with the experimental data, as indicated by R^2 ranging from 0.974 to 0.996.

Effects of Temperature, Soil Particle Fraction, and Salinity on Long-term Strength

Three approaches are commonly used to determine the long-term strength (σ_{lt}) of frozen soils from creep tests. The first involves relating a selected time (t_s), *e.g.*, service life of structures, to the secondary or minimum strain rate ($\dot{\epsilon}_m$) and failure strain (ε_f) (Ladanyi and Johnston 1974;

Andersland and Ladanyi 2003). The second method specifies an allowable secondary creep rate as a criterion for defining long-term strength (Vyalov et al. 1969). The third approach relates the time to failure (t_f) and the applied stress to create a long-term strength curve, as illustrated in Figure 9 (Tsytovich 1975).

Approaches 1 and 2 rely on the stress-strain rate relationship of frozen soil. Over the long term, these approaches assume that the creep response of frozen soil is dominated by secondary creep and primary creep contributes negligibly to the total strain (Vialov 1959). This assumption aligns with the “lifetime” concept, which states that the product of the minimum strain rate and the “lifetime” is a constant for frozen soil (Orth 1986; Cudmani et al. 2022; Schindler et al. 2024). “Lifetime” is defined as the time when the minimum creep rate is reached. Consequently, approaches 1 and 2 are particularly suitable for application to ice-rich permafrost in this study. The required stress-strain rate relationship for each undisturbed permafrost sample can be determined from multi-stage creep tests, as shown in Figure 8. The long-term strength is expressed by Eq. (3) (Ladanyi 1972; Andersland and Ladanyi 2003):

$$\begin{aligned} \sigma_{lt,a_1} &= \left(\frac{\epsilon_f}{t_s A}\right)^{1/n} \\ \sigma_{lt,a_2} &= \left(\frac{\dot{\epsilon}_m}{A}\right)^{1/n} \end{aligned} \tag{3}$$

where a_1 and a_2 represent approach 1 and approach 2, respectively. Approach 3 typically involves conducting single-stage creep tests on a series of identical specimens to construct a long-term strength curve (Vyalov 1969). Approach 3 is not applied in this study because: 1) the determination of time to failure depends on the failure point selection; 2) the long-term strength is not determined for each undisturbed permafrost sample; 3) the time to failure or "lifetime" depends on stress history (Schindler et al. 2024) and therefore the long-term strength curve determined from single-stage and multi-stage creep tests may vary.

We select 50 years as service life of structures (t_s) in approach 1 (Andersland and Ladnyi 2003) and an allowable secondary creep rate of 2.083×10^{-7} hr^{-1} (Vyalov et al. 1969) in approach 2. Table 3 presents the long-term strength estimates for the six permafrost samples.

Figure 10a illustrates the relationship between σ_{lt} and temperature. The average σ_{lt} of the six permafrost samples was 223 kPa at -10℃ and 25.7 kPa at -2℃. The average σ_{lt} decreased by 88.0% and 88.8% from -10℃ to -2℃ using approaches 1 and 2, respectively. Figure 10b shows the variation of σ_{lt} with θ_s at -10℃ and -2℃. At -10℃, σ_{lt} increased by 139.4 kPa (118.2%) and 196.4 kPa (120.5%) from θ_s = 0.14 to θ_s = 0.26 using approaches 1 and 2, respectively. Sample S4-5 deviated notably from the regression trend due to its higher salinity (5.4 ppt) compared to the average salinity (1.3 ppt) of the other samples. Solutes may have relatively large effects, even in low concentrations (Hooke et al. 1980). At -2℃, σ_{lt} showed a more gradual absolute increase with θ_s represented by a gently sloping trend line. This more gradual increase indicates that the strengthening effect of soil particles diminished at higher temperatures.

Stress-Strain Relationships under the UCS Tests

Figure 11 contains the UCS stress-strain responses of six permafrost samples at -2℃ and -10℃. The peak compressive strengths (σ_m) of the six samples were 0.84 MPa (S3-4), 3.56 MPa (S3-5), 0.83 MPa (S3-6), 3.23 MPa (S3-7), 1.23 MPa (S4-5), and 4.33 MPa (S5-3). σ_m represents the maximum stress permafrost can sustain before failure under high strain rate conditions over a short period compared to the CSC tests. Therefore, σ_m is the short-term strength of permafrost. As the temperature decreased, σ_m increased. At both temperatures, the samples with the lower soil particle fraction (θ_s = 0.14 to 0.29) behaved as a brittle material with a failure strain of about 1% soon after plastic yielding. The samples became ductile at higher θ_s of 0.41 to 0.43 with no significant change between yield strength and peak strength resulting from strain hardening.

Effects of Temperature, Soil Particle Fraction, and Salinity on Short-Term Strength

Figure 12a is a plot of $\log \sigma_m$ versus $\log T/T_0$, where T_0 is the reference temperature of -1°C. The circular data points represent test results from the current study. The square data points represent previous studies on remolded frozen soil (Zhu and Carbee, 1984). The peak compressive strength as a function of temperature is expressed as (Sayles and Haines, 1974a):

$$\sigma_m = B\left(\frac{T}{T_0}\right)^m \tag{4}$$

where B is an empirical parameter with the dimension of stress, and m is a dimensionless parameter. The short-term strength of the permafrost with $\theta_{s,avg}$ of 0.28 in the current study is consistently lower than that in Zhu and Carbee (1984) with $\theta_{s,avg}$ of 0.45. This result aligns with previous research that increasing soil particle fraction enhances the compressive strength of frozen soils (Goughnour and Andersland 1968; Baker 1979; Baker and Konrad 1985; Schindler et al. 2023). Figure 12b presents the relationship between σ_m and θ_s for the current study with salinity represented by color gradient. The compressive strength showed no clear correlation with soil particle fraction in this study. This lack of correlation can be attributed to the influence of salinity.

Permafrost with high θ_s exhibited high salinity, which can diminish the effect of soil particle fraction.

Soil Freezing Characteristic Curve (SFCC)

Based on laboratory testing, the soil freezing characteristic curve can be expressed using a simple power law (Anderson and Tice 1973):

$$\theta_{n,u} = C\left(\frac{T}{T_0}\right)^b \tag{5}$$

where $\theta_{n,u}$ is the normalized volumetric unfrozen water content by the total volumetric water content (θ_w), T_0 is the reference temperature of -1℃, and C and b are two experimentally-determined parameters of the power law model. Table 4 summarizes the results of gravimetric UWC of the 12 permafrost samples as a function of temperature ranging from -20℃ to 10℃. As expected, the gravimetric UWC increased with rising sub-freezing temperatures and eventually approached the total gravimetric water content, w, once the temperature exceeded 0℃.

Based on the results in Table 4, the volumetric UWC (θ_u) is calculated and normalized by total volumetric water content (θ_w) to range between 0 to 1. Using the power law model of SFCC (Eq. 5), we determine the parameters, C and b, by correlating temperature with the normalized UWC. Figure 13 depicts the experimental results for the SFCC of all samples. The dashed lines represent the best-fit models. The power law models demonstrate a robust correlation with the experimental data, evidenced by R^2 values ranging from 0.969 to 0.998.

Development of Prediction Models

Effect of Temperature and Soil Particle Fraction on Secondary Creep Parameters

Data in this study are combined with the data in the literature to further understand how soil particle fraction and temperature affect secondary creep parameters. Figure 14 presents a scatter plot of 29 data points and illustrates the relationships among *A*, *n*, soil particle fraction, and temperature. The temperature factor is defined as $1/(1+|T|)$ (Voytkovskiy 1960), where $|T|$ is the absolute value of temperature. The circular data points represent test results from the current study. The triangle and square data points represent the data from previous studies (Bray 2012, 2013).

Figure 10 highlights the interactive effects of soil particle fraction and temperature on the strength of permafrost. Using the combined dataset, we perform a multilinear regression analysis with an interaction term to investigate the relationship between soil particle fraction, temperature, and secondary creep parameters. Details of the statistical analysis and combined dataset (Table S2) are provided in the supplementary materials. Figure 14a illustrates the regression surface for creep parameter *A* as modeled by the multilinear regression; parameter *A* is represented in logarithmic scale. Figure 14b presents the regression surface for creep parameter *n*. *A* decreases with an increase soil particle fraction. This decrease becomes more pronounced at lower sub-freezing temperatures, characterized by a faster decline in parameter *A* with increasing soil particle fraction. The decrease of A indicates increased creep resistance with increasing viscosity. *A* also increases with rising sub-freezing temperatures, with this effect being more pronounced at higher soil particle fractions. The creep parameter *n* increases with an increase in soil particle fraction, and this trend is more noticeable under colder temperature conditions. The increase in *n* indicates an increased nonlinear relationship between axial stress and minimum strain rate, wherein the minimum strain rate increases rapidly with higher axial stress. As the sub-freezing temperature increases, parameter *n* decreases, but this decrease is less marked at lower soil particle fractions. Theoretically, parameter *n* stabilizes at a constant value of 3 for polycrystalline ice irrespective of the sub-freezing temperature (Glen 1955; Morgenstern et al. 1980).

We establish the relationship (Eq. 6) between creep parameter *A* and soil particle fraction and temperature by plotting ln *A* against $1/(1+|T|)$ and θ_s. Similarly, we establish the relationship (Eq. 7) between creep parameter *n* and $1/(1+|T|)$ and θ_s. Consequently, Glen's flow model (Eq. 2) of ice-rich permafrost as a function of soil particle fraction and temperature is expressed in Eq. 8.

$$\ln A = -14.1 - 154.1\theta_s + \frac{186.9}{1+|T|}\theta_s \tag{6}$$

$$n = 1.4 + 20.1\theta_s - \frac{19.6}{1+|T|}\theta_s \tag{7}$$

$$\dot{\epsilon}_m = \exp[-14.1 - 154.1\theta_s + \frac{186.9}{1+|T|}\theta_s]\,\sigma^{1.4+20.1\theta_s-\frac{19.6}{1+|T|}\theta_s} \tag{8}$$

$$0.15 \leq \theta_s \leq 0.45; -10℃ \leq T \leq -1℃$$

The regression analysis yielded adjusted R^2 values of 0.87 for parameter *A* and 0.83 for parameter *n*, with corresponding RMSE of 4.8 and 0.7, respectively. This semi-empirical model is developed based on experimental data with a soil particle fraction between 14% to 46% and temperature between -10℃ to -0.77℃. The ranges of the parameters represent typical ice-rich permafrost with near-surface ground temperature profiles in northern Alaska.

Effect of Salinity and Soil Particle Fraction on the Parameters of SFCC Model

Solute concentration and soil particle fraction influence unfrozen water content (Hivon and Sego 1995; Suzuki 2004; Watanabe and Wake 2009; Wu et al. 2015). Both solute concentration and soil particle fraction may affect the mechanisms of soil freezing point depression. These mechanisms include capillarity in small pores, adsorption on mineral surfaces, and the presence of dissolved salts in pore water (Dou et al. 2016). The effects of salinity and soil particle fraction on the parameters *C* and *b* of the SFCC model were analyzed using multilinear regression based on the UWC data presented in Table 4. Figure 15 illustrates the variation of the parameters of SFCC model, *C* and *b*, with their corresponding soil particle fraction and salinity.

The parameters *b* and *C* in relation to soil particle fraction and salinity are formulated in Eq. (9) to (10). In Eq. (9), salinity, *S*, is transformed to natural logarithmic scale to linearize the relationship, thereby improving the fit of the model. Eq. (11) shows the equation to calculate $\theta_{n,u}$.

$$b = -0.4 - 0.15 \ln S \tag{9}$$

$$C = 0.03 + 0.01S + 0.06S\theta_s \tag{10}$$

$$\begin{gathered} \theta_{n,u} = (0.03 + 0.01S + 0.06S\theta_s)T^{-0.40-0.15\ln S} \\ 0.15 \le \theta_s \le 0.45;\ 0.5\,ppt \le S \le 15\,ppt \end{gathered} \tag{11}$$

Regression analysis results in adjusted R^2 values of 0.83 for *b* and 0.97 for *C*, with RMSE of 0.08 and 0.04, respectively. This mathematical description for SFCC is based on experimental data with a soil particle fraction range from 14% to 59% and a salinity range from 0.5 to 15.2 ppt.

Using Eq. 11, volumetric unfrozen water content (θ_u) can be calculated by multiplying $\theta_{n,u}$ with θ_w. Figure 16 illustrates the effect of soil particle fraction on θ_u for ice-rich silty sand at two salinities, 2 ppt and 15 ppt. As expected, higher salinity results in higher θ_u. At both salinities, θ_u is nearly independent of the soil particle fraction, with slightly higher θ_u observed at higher soil particle fraction under 15 ppt salinity. This observation indicates that soil particle fraction has little effect on θ_u in ice-rich silty sand. This weak effect can be attributed to the limited adsorption ability of sand (Zhang and Lu 2021; Wang and Hu 2023).

Model Performance Evaluation

Figure 17 presents the density scatter plot comparing the measured and calculated data. Kernel density estimate was used to obtain the spatial density of data points and was represented by the color gradient. Figure 17a compares the measured and calculated minimum strain rate ($\dot{\epsilon_m}$) using Eq. (8). Figure 17b compares the measured and calculated normalized unfrozen water content ($\theta_{n,u}$) using Eq. (11). The 242 measured data points on $\dot{\epsilon_m}$ are collected from this research and previous studies (Bray 2012; Bray 2013) within the tested stress range. The experimental data are available in Table S3 of the supplementary materials. The 84 data points on $\theta_{n,u}$ are calculated based on measured gravimetric unfrozen water content summarized in Table 4. The semi-empirical models demonstrate reasonable reproductions of the experimental data on both $\dot{\epsilon_m}$ and $\theta_{n,u}$. The robust correlations are evidenced by the overall correlation factor (R^2) of 0.9 and 0.88 for $\dot{\epsilon_m}$ and $\theta_{n,u}$, respectively.

Influence of Temperature and Unfrozen Water Content on the Effect of Soil Particle Fraction

Figure 18 illustrates the variations in minimum strain rate ($\dot{\epsilon_m}$) with temperature (T), soil particle fraction (θ_s), and axial stress (σ_1) using Eq. (8). The results show that the influence of soil particles on strain rate diminishes as temperature increases (Figure 18a). The effect of temperature on strain rate becomes more pronounced at higher soil particle fractions (Figure 18b). Furthermore, the effect of temperature on strain rate remains consistent across varying axial stress levels at a constant soil particle fraction (Figure 18c). Unlike the earlier model that predicted equidistant curves (Arenson and Springman 2005), this semi-empirical model captures the interactive effects of soil particle fraction and temperature observed in laboratory testing.

The interactive effects of soil particle fraction and temperature on minimum strain rate can be attributed to the increase of unfrozen water content. To quantify the role of unfrozen water content in creep deformation, the established SFCC model (Eq. 11) is used to investigate the effect of θ_u on Glen's flow law parameters A and n, as shown in Figure 19. The discrete points are calculated based on the index properties of the tested samples. The lines are obtained using the relationships between temperature and soil particle fraction with parameters A, n (Eq. 6 and 7), and θ_u (Eq. 11) at three soil particle fractions.

The general trend in Figure 19 indicates that with increasing θ_u, A increases and n decreases. This trend becomes more pronounced at higher soil particle fractions. With increasing θ_u, the differences between the parameters A and n converge across varying soil particle fractions. This observation suggests that increasing unfrozen water content diminishes the influence of soil particle fraction on creep deformation even though the amount of unfrozen water is independent of soil particle fractions (Figure 16) at the same sub-freezing temperature.

Long-Term Strength Prediction of Ice-Rich Permafrost

In northern Alaska, ice-rich permafrost exists under varying soil particle fraction and temperature conditions. The proposed semi-empirical equation for secondary creep rate (Eq. 8) can quantitatively predict the long-term strength of permafrost. Figure 20 presents the long-term strength predictions incorporating the effects of soil particle fraction and temperature. Figure 20a illustrates approach 1 predictions assuming a 50-year service life with ε_f = 0.1, 0.05, and 0.02. Figure 20b shows approach 2 prediction with an allowable secondary creep rate of 2.083×10^{-7} hr^{-1} (Vyalov et al. 1969). The predictions align with the experimental observations: long-term strength increases with higher θ_s and lower temperatures. The strengthening effect of soil particles is more pronounced at lower temperatures but diminishes as temperatures rise.

Figure 21 shows a conceptual diagram illustrating the mechanism of the interactive effects of soil particle fraction, unfrozen water content, temperature, and salinity on creep deformation and long-term strength of ice-rich permafrost at the particle scale. Soil particles hinder creep deformation and increase the long-term strength. As a result, the increase in soil particle fraction shows a strengthening effect at colder temperatures and lower salinity. The unfrozen water content significantly increases with temperature and salinity near the melting point. The increase in unfrozen water content diminishes the strengthening effect of soil particle fraction. Therefore, the increase in soil particle fraction shows a reduced strengthening effect on creep resistance of permafrost at warmer temperatures and higher salinity.

Discussion

Multi-Stage Creep Tests Versus Single-Stage Creep Tests

The multi-stage creep tests were conducted in this study. Unlike single-stage tests applying constant stress until failure, multi-stage tests involve stepped increased stress to investigate the creep response of a single specimen over multiple stress levels. This approach prevents the termination of tests at a non-informative stress level and maximizes data collection from each specimen. Therefore, this approach is particularly useful when the creep strength of the material is unknown before the tests. Because undisturbed permafrost samples of sufficient quality are limited, multi-stage testing also offers a practical advantage: it reduces the total number of specimens required compared to single-stage testing.

Under multi-stage creep tests, the secondary creep rate for a given stress magnitude remains independent of both the stress history and strain path that lead to the secondary creep rate (Eckardt 1979; Bray 2013; Schindler et al. 2023). Figure 22 illustrates a conceptual diagram of secondary creep conditions under single-stage and multi-stage stress scenarios. In secondary creep phase, the strain paths remain parallel in both stress scenarios at the same stress magnitude. The secondary creep rate is the same for a given stress magnitude regardless of whether the stress is applied in a single stage or through multiple stages.

Limitations of This Study

The data, equations, and discussions presented in this paper are based on limited laboratory results for ice-rich permafrost under uniaxial stress conditions. The mathematical models presented in this study can reproduce the experimental data to a certain extent. Further experimental, analytical, and numerical studies are recommended to investigate the proposed mechanisms and relationships. Several uncertainties should be expected during the interpretation of the observed mechanisms. First, the creep response of permafrost is influenced by the distribution and orientation of ice. The heterogeneous distribution of ice in permafrost can lead to high variability in the results. Second, the semi-empirical model (Eq. 8) used to calculate the minimum strain rate should be applied cautiously at high axial stress. At high axial stress (e.g., 1379 kPa at -10℃), permafrost may transition directly into tertiary creep without well-defined primary and secondary creep stages. Third, the experimental data and model were based on saturated permafrost sampled from the Arctic Coastal Plain. However, presence of air in permafrost can affect its creep mechanism by influencing the ice structure, pore pressure, and temperature variations.

Summary and Conclusions

This paper aims to characterize the geophysical and geomechanical properties of undisturbed permafrost in northern Alaska and to investigate the interactive effects of soil particle fraction, unfrozen water content, temperature, and salinity on creep deformation and long-term strength. A geotechnical investigation of near-surface permafrost soils (upper 1.5 m) sampled near Utqiaġvik, Alaska was first carried out for geotechnical characterization. The experimental approach included constant stress creep tests, unconfined compressive strength tests, and unfrozen water content tests. This research yields the following key conclusions:

- The permafrost at shallow depths in the tundra near Utqiaġvik, Alaska was characterized as saline ice-rich silty sand and non-uniformly distributed ice.
- The average long-term strength of the tested permafrost was 223 kPa at -10℃ and 25.7 kPa at -2℃. The long-term strength decreased by nearly 90% from -10℃ to -2℃. At -10℃,

the long-term strength increased by approximately 120% as the soil particle fraction rose from 0.14 to 0.26. The strengthening effect of soil particles diminished at higher salinity and at a higher temperature of -2℃.

- The compressive strength showed no clear correlation with soil particle fraction in this study. This lack of correlation can be attributed to the influence of salinity.
- The effect of volumetric soil particle fraction on secondary creep rate depends on temperature.
- Unfrozen water content is independent of the soil particle fraction in ice-rich silty sand.
- Increasing unfrozen water content diminishes the influence of soil particle fraction on creep deformation.
- A quantitative tool is developed to predict the long-term strength of ice-rich permafrost, incorporating the effects of soil particle fraction and temperature.

Data availability statement: Some or all data, models, or code that support the findings of this study are available from the corresponding author upon reasonable request.

Acknowledgements: Z.W., M.X., J.H. were supported by the U.S. National Science Foundation (NSF) (grant number: RISE-1927718). M.X. was also supported by NSF (grant numbers: OISE-1927137, OPP-1945369).

Notation

The following symbols are used in this paper:

$\dot{\epsilon}_1$ = Axial strain rate;

$\dot{\epsilon}_{avg}$ = Moving average of strain rate;

$\dot{\epsilon}_m$ = Minimum strain rate/secondary creep rate;

ϵ_1 = Axial strain;

ϵ_f = Failure strain;

G_s = Specific gravity;

T_0 = Reference temperature;

t_f = Time to failure;

t_s = Service life of structures;

$\theta_{n,u}$ = Normalized unfrozen water content;

$\theta_{s,avg}$ = Average volumetric soil particle fraction;

θ_s = Volumetric soil particle fraction;

θ_u = Volumetric unfrozen water content;

θ_w = Total volumetric water content;

ρ_{bf} = Bulk frozen density;

ρ_d = Dry density;

σ_1 = Axial stress;

σ_{lt} = Long-term strength;

σ_m = Peak compressive strength;

A = fluidity parameter;

B = Empirical parameter for unconfined compressive strength;

C = Empirical parameter for unfrozen water content;

S = Salinity;

T = Temperature;

b = Exponent for unfrozen water content;

m = Stress exponent for unconfined compressive strength;

n = Stress exponent of Glen’s flow law;

t = Time; and

w = Total gravimetric water content.

Supplemental Materials

Tables S1, S2, S3 and Figures S1, S2 are available online in the ASCE Library (ascelibrary.org).

References

Andersland, O. B., and B. Ladanyi. 2003. *Frozen ground engineering*. 2nd ed. New York: Wiley.

Anderson, D. M., and Tice, A. R. (1973). "The unfrozen interfacial phase in frozensoil water systems." *Ecological studies, analysis and synthesis, vol. 4.*, A. Hadas, ed., Springer-Verlag, Berlin, West Germany.

Anisimov, O. A., and Nelson, F. E. 1996. "Permafrost distribution in the Northern Hemisphere under scenarios of climatic change." *Global Planet Change.* 14(1-2): 59-72. https://doi.org/10.1016/0921-8181(96)00002-1.

Arenson, L. U., and Springman, S. M. 2005a. "Triaxial constant stress and constant strain rate tests on ice-rich permafrost samples." *Can Geotech J*. 42(2): 412-430. https://doi.org/10.1139/t04-111.

Arenson, L. U., and Springman, S. M. 2005b. "Mathematical descriptions for the behaviour of ice-rich frozen soils at temperatures close to 0 °C." *Can Geotech J*. 42(2): 431-442. https://doi.org/10.1139/t04-109.

Arenson, L. U., Johansen, M. M., and Springman, S. M. 2004. "Effects of volumetric ice content and strain rate on shear strength under triaxial conditions for frozen soil samples." *Permafr Periglac Process*. 15(3): 261-271. https://doi.org/10.1002/ppp.498.

ASTM International. 2006. *Standard test method for laboratory determination of strength properties of frozen soil at a constant rate of strain* (D 7300-06). West Conshohocken, PA: ASTM International. https://doi.org/10.1520/D7300-06.

ASTM International. 2006. *Standard test method for sieve analysis of fine and coarse aggregates* (C 136). West Conshohocken, PA: ASTM International. https://doi.org/10.1520/C0136.

ASTM International. 2007. *Standard test method for particle-size analysis of soils* (D422-63). West Conshohocken, PA: ASTM International. https://doi.org/10.1520/D0422-63.

ASTM International. 2017. *Standard test methods for liquid limit, plastic limit, and plasticity index of soils* (D 4318-17e1). West Conshohocken, PA: ASTM International. https://doi.org/10.1520/D4318-17E1.

Baker, T. H. W. 1979. "Strain rate effect on the compressive strength of frozen sand. " *Eng. Geol*. 13 (1): 223–231. https://doi.org/10.1016/0013-7952(79)90034-6.

Baker, T.H. W., Konrad, J.M. 1985. "Effect of sample preparation on the strength of artificially frozen sand. " In: *Proceedings of the 4th international symposium on ground freezing*, Sapporo, 2: 171–176.

Biskaborn, B. K., Smith, S. L., Noetzli, J., Matthes, H., Vieira, G., Streletskiy, D. A., et al. "Permafrost is warming at a global scale." *Nat Commun*. 10. https://doi.org/10.1038/s41467-018-08240-4.

Bray, M. T. 2012. “The influence of cryostructure on the creep behavior ofice-rich permafrost.” Cold Regions Sci. Technol. 79: 43–52. https://doi.org/10.1016/j.coldregions.2012.04.003.

Bray, M. T. 2013. "Secondary creep approximations of ice-rich soils and ice using transient relaxation tests." Cold Regions Sci. Technol. 88: 17-36. https://doi.org/10.1016/j.coldregions.2012.12.011.

Creel, R., Guimond, J., Jones, B. M., Nielsen, D. M., Bristol, E., Tweedie, C. E., and Overduin, P. P. 2024. "Permafrost thaw subsidence, sea-level rise, and erosion are transforming Alaska's Arctic coastal zone." *P Natl Acad Sci*. 121(50). https://doi.org/10.1073/pnas.2409411121.

Cudmani, R., Yan, W., and Schindler, U. 2023. "A constitutive model for the simulation of temperature-, stress- and rate-dependent behaviour of frozen granular soils." *Géotechnique*. 73(12): 1043-1055. https://doi.org/10.1680/jgeot.21.00012.

Dou, S., Nakagawa, S., Dreger, D., and Ajo-Franklin, J. 2016. "A rock-physics investigation of unconsolidated saline permafrost: P-wave properties from laboratory ultrasonic measurements." *Geophysics*. 81(1): WA233-WA245. https://doi.org/10.1190/geo2015-0176.1.

Duval, P., (1977). *The role of water content on the creep rate of polycrystalline ice*. IUGG General Assembly of Grenoble, Aug./Sep. 1975. IAHS Publ. No. 118, pp. 29-33.

Eckardt, H. 1979. "Creep behaviour of frozen soils in uniaxial compression tests." *Eng. Geol*. 13(1-4): 185-195. https://doi.org/10.1016/0013-7952(79)90031-0.

Glen, J. W., and Perutz, M. F. 1955. "The creep of polycrystalline ice." *P Roy Soc A-Math Phy*. 228(1175): 519-538. https://doi.org/10.1098/rspa.1955.0066.

Goughnour, R. R., and Andersland, O. B. 1968. "Mechanical Properties of a Sand-Ice System." *J. Soil Mech. Found. Div*. 94(4): 923-950. https://doi.org/10.1061/JSFEAQ.0001179.

Hivon, E. G., and Sego, D. C. 1995. "Strength of frozen saline soils." *Can Geotech J*. 32(2): 336-354. https://doi.org/10.1139/t95-034.

Hjort, J., Streletskiy, D., Doré, G., Wu, Q. B., Bjella, K., and Luoto, M. 2022. "Impacts of permafrost degradation on infrastructure." *Nat Rev Earth Env*. 3(1): 24-38. https://doi.org/10.1038/s43017-021-00247-8.

Hooke, R. L., Dahlin, B. B., and Kauper, M. T. 1972. "Creep of Ice Containing Dispersed Fine Sand." *J. Glaciol*. 11(63): 327-336. https://doi.org/10.3189/S0022143000022309.

Hooke, R. L., Mellor, M., Budd, W., Glen, J., Higashi, A., Jacka, T., Jones, S., Lile, R., Martin, R., and Meier, M. 1980. "Mechanical properties of polycrystalline ice: An assessment of current knowledge and priorities for research: Report prepared for the International Commission on Snow and Ice, with support from the US National Science Foundation." *Cold Reg Sci Technol*. 3(4): 263-275. https://doi.org/10.1016/0165-232X(80)90033-6.

ISO (International Organization for Standardization). 1994. *Soil quality—Determination of the specific electrical conductivity* (ISO 11265:1994). Geneva, Switzerland: ISO.

Kanevskiy, M., Shur, Y., Jorgenson, M.T., Ping, C.L., Michaelson, G.J., Fortier, D., Stephani, E., Dillon, M. and Tumskoy, V. 2013. "Ground ice in the upper permafrost of the Beaufort Sea coast of Alaska. " *Cold Reg Sci Technol*. 85 (Jan): 56-70. https://doi.org/10.1016/j.coldregions.2012.08.002.

Kruse, A. M., Darrow, M. M., and Akagawa, S. 2018. "Improvements in Measuring Unfrozen Water in Frozen Soils Using the Pulsed Nuclear Magnetic Resonance Method." *J. Cold Reg. Eng*. 32(1): 04017016. https://doi.org/10.1061/(ASCE)CR.1943-5495.0000141.

Ladanyi, B. 1972. "An Engineering Theory of Creep of Frozen Soils." *Can Geotech J*. 9(1): 63-80. https://doi.org/10.1139/t72-005.

Ladanyi, B., and Johnston, G. H. 1974. "Behavior of Circular Footings and Plate Anchors Embedded in Permafrost." *Can Geotech J*. 11(4): 531-553. https://doi.org/10.1139/t74-057.

Moore, P. L. 2014. "Deformation of debris-ice mixtures." *Rev. Geophys*. 52(3): 435-467. https://doi.org/10.1002/2014RG000453.

Morgenstern, N. R., Roggensack, W. D., and Weaver, J. S. 1980. "The Behavior of Friction Piles in Ice and Ice-Rich Soils." *Can Geotech J*. 17(3): 405-415. https://doi.org/10.1139/t80-047.

Nixon, J. F., and Lem, G. 1984. "Creep and strength testing of frozen saline fine-grained soils." *Can Geotech J*. 21(3): 518-529. https://doi.org/10.1139/t84-054.

Nixon, J. F., and McRoberts, E. C. 1976. "A design approach for pile foundations in permafrost." *Can Geotech J*. 13(1): 40-57. https://doi.org/10.1139/t76-005.

Orth, W. (1988). A creep formula for practical application based on crystal mechanics. In *Fifth International Symposium on Ground Freezing*, pages 205–211, Nottingham, UK.

Rantanen, M., Karpechko, A. Y., Lipponen, A., Nordling, K., Hyvärinen, O., Ruosteenoja, K., Vihma, T., and Laaksonen, A. 2022. "The Arctic has warmed nearly four times faster than the globe since 1979." *Commun Earth Environ*. 3(1). https://doi.org/10.1038/s43247-022-00498-3.

Sayles, F. H. 1968. *Creep of frozen sands*. Tech. Rep. No. CRREL-TR-190. Hanover, NH: Cold Regions Research and Engineering Lab.

Sayles, F. H. 1974b. "Triaxial and creep tests on frozen Ottawa sand. " In *Proc., North American Contribution to the 2nd Int. Permafrost Conf.,* 384–391. Washington, DC: National Academy of Sciences.

Sayles, F. H., and D. Haines. 1974a. *Creep of Frozen Silt and Clay*. Tech. Rep. No. CRREL-TR-252. Hanover, NH: Cold Regions Research and Engineering Lab.

Schindler, U., Chrisopoulos, S., Yan, W., and Cudmani, R. 2023. "Tunnel excavations supported by frozen soil bodies: Lab testing and modelling. " In *Expanding Underground-Knowledge and Passion to Make a Positive Impact on the World*. CRC Press. 895–903. https://doi.org/10.1201/9781003348030-108.

Schindler, U., Cudmani, R., Chrisopoulos, S., and Schünemann, A. 2024. "Multi-stage creep behavior of frozen granular soils: experimental evidence and constitutive modeling." *Can Geotech J*. 61(1): 118-133. https://doi.org/10.1139/cgj-2022-0637.

Shastri, A., Sánchez, M., Gai, X. R., Lee, M. Y., and Dewers, T. 2021. "Mechanical behavior of frozen soils: Experimental investigation and numerical modeling." *Comput Geotech*. 138. https://doi.org/10.1016/j.compgeo.2021.104361.

Shelman, A., Tantalla, J., Sritharan, S., Nikolaou, S., and Lacy, H. 2014. "Characterization of Seasonally Frozen Soils for Seismic Design of Foundations." *J Geotech Geoenviron*. 140(7). https://doi.org/10.1061/(Asce)Gt.1943-5606.0001065.

Suzuki, S. 2004. "Dependence of unfrozen water content in unsaturated frozen clay soil on initial soil moisture content." *Soil Sci. Plant Nutr*. 50 (4): 603–606. https://doi.org/10.1080/00380768.2004.10408518.

Thompson, E. G., and Sales, F. H. 1972. "In Situ Creep Analysis of Room in Frozen Soil." *J. Soil Mech. Found. Div*. 98(9): 899-915. https://doi.org/10.1061/JSFEAQ.0001780.

Ting, J. M., Martin, R. T., and Ladd, C. C. 1983. "Mechanisms of Strength for Frozen Sand." *J. Geotech. Eng*. 109(10): 1286-1302. https://doi.org/10.1061/(ASCE)0733-9410(1983)109:10(1286).

Tourei, A., Ji, X., Rocha dos Santos, G., Czarny, R., Rybakov, S., Wang, Z., Hallissey, M., Martin, E. R., Xiao, M., Zhu, T., Nicolsky, D., and Jensen, A. 2024. "Mapping Permafrost Variability and Degradation Using Seismic Surface Waves, Electrical Resistivity, and Temperature Sensing: A Case Study in Arctic Alaska." *J. Geophys. Res. Earth Surf*. 129(3): e2023JF007352. https://doi.org/10.1029/2023JF007352.

Tsytovich, N. A. (1975). *The mechanics of frozen ground*. McGraw-Hill, Inc., NewYork, N.Y.

Vialov, S. S. 1959. *Rheological properties and bearing capacity of frozen soils*. Hanover, NH: US Army Cold Regions Research and Engineering Laboratory.

Voytkovskiy, K.F. 1960. "Mekjanicheskiye svoystva lda. Izvestiya Akademii Nauk, Moscow." [The mechanical properties of ice. U.S. Air Force Cambridge Research Laboratory, Bedford, Mass., translation No. AFCRL-62–838.]

Vyalov, S. 1986. "Rheological fundaments of soil mechanics." In Vol. 36 of *Developments in geotechnical engineering*. Amsterdam, Netherlands: Elsevier.

Vyalov, S. S., 1969, "Methods of Determining Creep, Long-term Strength and Compressibility Characteristics of Frozen Soils," (from Russian) Technical Translation 1364, National Research Council of Canada, Ottawa, Canada.

Wang, J. H., Zhang, F., Yang, Z., and Yang, P. 2022. "Experimental investigation on the mechanical properties of thawed deep permafrost from the Kuparuk River Delta of the North Slope of Alaska." *Cold Reg Sci Technol*. 195. https://doi.org/10.1016/j.coldregions.2022.103482.

Wang, Y., and Hu, L. 2023. "A Theoretical Model of Soil Freezing Characteristic Curve Considering the Freezing of Adsorbed Water and Capillary Water." *Water Resour. Res*. 59(7): e2023WR034662. https://doi.org/10.1029/2023WR034662.

Wang, Z., Xiao, M. and Bray, M. "Cryostructure and Uniaxial Compressive Strength of Ice-Rich Permafrost in Northern Alaska." *Proceedings of the 20th International Conference on Cold Regions Engineering (ICCRE)*, 295-307. Anchorage, Alaska, May 13 - 16, 2024. *Cold Regions Engineering 2024: Sustainable and Resilient Engineering Solutions for Changing Cold Regions*. American Society of Civil Engineers. https://doi.org/10.1061/9780784485460.027.

Wang, Z., Xiao, M., Bray, M. and Darrow, M. "Experimental Investigation of Thermal and Hydraulic Properties of Ice-Rich Saline Permafrost in Northern Alaska." *Proceedings of the 20th International Conference on Cold Regions Engineering (ICCRE)*, 285-294. Anchorage, Alaska, May 13 - 16, 2024. *Cold Regions Engineering 2024: Sustainable and Resilient Engineering Solutions for Changing Cold Regions*. American Society of Civil Engineers. https://doi.org/10.1061/9780784485460.026.

Wang, Z., Xiao, M., Liew, M., Jensen, A., Farquharson, L., Romanovsky, V., Nicolsky, D., McComb, C., Jones, B.M., Zhang, X. and Alessa, L. 2023a. "Arctic geohazard mapping tools for civil infrastructure planning: a systematic review." *Cold Reg Sci Technol*. (Jul.): 103969. https://doi.org/10.1016/j.coldregions.2023.103969.

Wang, Z., Xiao, M., Nicolsky, D., Romanovsky, V., McComb, C. and Farquharson, L. 2023b. "Arctic coastal hazard assessment considering permafrost thaw subsidence, coastal erosion, and flooding." *Environ. Res. Lett*. 18(10): 104003. https://doi.org/10.1088/1748-9326/acf4ac.

Watanabe, K., and T. Wake. 2009. “Measurement of unfrozen water content and relative permittivity of frozen unsaturated soil using NMR and TDR.” *Cold Reg. Sci. Technol*. 59 (1): 34–41. https://doi.org/10 .1016/j.coldregions.2009.05.011.

Weaver, J. S., and Morgenstern, N. R. 1981. "Pile Design in Permafrost." *Can Geotech J*. 18(3): 357-370. https://doi.org/10.1139/t81-043.

Wilson, F. H., Hults, C. K., Mull, C. G. and Karl, S. M. 2015. "Geologic map of Alaska (Scientific Investigations Map 3340) ." *U.S. Geological Survey*. https://doi.org/10.3133/sim3340.

Wu, M., X. Tan, J. Huang, J. Wu, and P.-E. Jansson. 2015. “Solute and water effects on soil freezing characteristics based on laboratory experiments.” *Cold Reg. Sci. Technol*. 115 (Jul): 22–29. https://doi.org/10.1016/j.coldregions.2015.03.007.

Yang, Z. H., Still, B., and Ge, X. X. 2015. "Mechanical properties of seasonally frozen and permafrost soils at high strain rate." *Cold Reg Sci Technol*. 113: 12-19. https://doi.org/10.1016/j.coldregions.2015.02.008.

Zhang, C., and Lu, N. 2021. "Soil Sorptive Potential–Based Paradigm for Soil Freezing Curves." *J Geotech Geoenviron*. 147(9): 04021086. https://doi.org/10.1061/(ASCE)GT.1943-5606.0002597.

Zhu, Y. L., and Carbee, D. L. 1984. "Uniaxial Compressive Strength of Frozen Silt under Constant Deformation Rates." *Cold Reg Sci Technol*. 9(1): 3-15. https://doi.org/10.1016/0165-232X(84)90043-0.

Zhu, Y.L., and Carbee, D. L. 1987. "Tensile strength of frozen silt." *U.S. Army CRREL Report 87-15,* Corps of Engrs., Cold Regions Res. and Engrg. Lab., Hanover, N.H.

Figure Captions

Fig. 1. Field sampling map: (a) Utqiaġvik, North Slope Borough, Alaska (world borders data from World Countries Generalized, Esri); (b) study region; (c) aerial views of the five permafrost sampling locations (base map data from imagery copyright 2022 Maxar).

Fig. 2. Cryostratigraphy of Arctic coastal plain deposits at the five sampling locations: (a) location S1; (b) location S2; (c) location S3; (d) location S4; and (e) location S5. The cryostructure classification system follows Kanevskiy et al. (2013).

Fig. 3. Selected permafrost cores for laboratory testing.

Fig. 4. Grain-size distributions of tested samples.

Fig. 5. Test setup and sample placement: (a) UCS test and (b) CSC test.

Fig. 6. Creep behavior from multi-stage constant stress creep tests: (a) axial strain vs. time at -2℃; (b) axial strain rate vs. time at -2℃; (c) axial strain vs. time at -10℃; (d) axial strain rate vs. time at -10℃.

Fig. 7. Determination of minimum creep strain rate: (a) S4-3 at -2℃; (b) S4-2 at -10℃.

Fig. 8. Stress-strain rate relationships: (a) at -2℃ and (b) at -10℃.

Fig. 9. Determination of the long-term strength curve for frozen soil.

Fig. 10. Long-term strength of the permafrost at varying soil particle fraction, temperature, and salinity: (a) σ_{lt} vs. temperature; (b) σ_{lt} vs. θ_s.

Fig. 11. Stress-strain response of permafrost samples during UCS tests: (a) axial stress vs. axial strain at -2℃; (b) axial stress vs. axial strain at -10℃.

Fig. 12. Effect of soil particle fraction, temperature, and salinity on peak compressive strength: (a) $\log(\sigma_m)$ vs. $\log(T/T_0)$; (b) σ_m vs. θ_s at varying salinity.

Fig. 13. Relationship between normalized volumetric UWC ($\theta_{n,u}$) and temperature.

Fig. 14. Multilinear regression analysis for creep parameters: (a) regression surface for creep parameter A; (b) regression surface for creep parameter n.

Fig. 15. Multilinear regression analysis for SFCC parameters: (a) regression surface for parameter b; (b) regression surface for parameter C.

Fig. 16. Effect of soil particle fraction on volumetric unfrozen water content (θ_u) at salinity of 2 and 15 parts per thousand (ppt) for ice-rich silty sand.

Fig. 17. Comparison between experimental data and model predictions: (a) minimum strain rate; (b) normalized unfrozen water content.

Fig. 18. Variations of minimum strain rate as a function of temperature (T), soil particle fraction (θ_s), and axial stress (σ_1).

Fig. 19. Effect of unfrozen water content on parameters of Glen's flow law at different soil particle fractions: (a) parameter A vs. unfrozen water content; (b) parameter n vs. unfrozen water content.

Fig. 20. Long-term strength predictions incorporating the effects of soil particle fraction and temperature: (a) approach 1 assuming a 50-year service life with ε_f = 0.1, 0.05, and 0.02; (b) approach 2 with an allowable secondary creep rate of 2.083×10^{-7} hr^{-1}.

Fig. 21. Conceptual diagram illustrating the particle-scale mechanism of the interactive effects of soil particle fraction, unfrozen water content, temperature, and salinity on creep deformation and long-term strength.

Fig. 22. Conceptual diagram illustrating secondary creep conditions under single-stage and muti-stage stress scenarios (adapted from Bray 2013).

Tables

Table 1. Summary of physical properties of tested samples. ρ_{bf} is bulk frozen density, ρ_{dry} is dry density, w is total gravimetric water content, θ_s is the volumetric soil particle fraction, θ_w is total volumetric water content in the thawed state, LL is liquid limit, PI is plasticity index, and G_s is specific gravity.

Sample No.	Test	Depth (cm)	ρ_{bf} (g/cm^3)	ρ_{dry} (g/cm^3)	w (%)	θ_s (%)	θ_w (%)	Salinity (ppt)	LL	PI	G_s
S2-4	UWC	105-113	1.38	0.73	89.1	29.1	69.1	9.42	N/A	N/A	2.51
S2-5	UWC	130-137	1.22	0.84	45.1	58.6	39.3	15.24	N/A	N/A	1.43
S3-3	UWC	72-81	1.28	0.71	80.4	37.8	60.2	2.16	N/A	N/A	1.88
S3-4	UCS	81-89	1.45	0.91	59.0	41.3	56.6	4.04	26	2	2.21
S3-5*	UCS	92-100	1.57	1.05	50.1	42.8	55.0	5.45	26	1	2.44
S3-6*	UCS	114-122	1.38	0.73	89.5	28.9	69.3	4.10	20	1	2.52
S3-7	UWC	135-141	1.37	0.71	93.8	27.7	70.6	3.79	N/A	N/A	2.55
S3-7	UCS	146-155	1.23	0.49	149.7	19.6	79.0	1.77	22	1	2.52
S4-2*	CSC	52-61	1.16	0.43	171.5	20.1	78.5	0.84	26	3	2.13
S4-2	CSC	61-70	1.24	0.56	121.0	25.9	72.4	1.06	21	1	2.16
S4-3*	CSC	65-74	1.32	0.65	103.3	26.8	71.4	1.36	20	1	2.42
S4-3	UWC	74-81	1.39	0.70	98.4	24.8	73.5	2.22	N/A	N/A	2.83
S4-3	CSC	84-93	1.15	0.36	219.1	13.9	85.1	2.14	22	1	2.60
S4-4	CSC	99-108	1.28	0.53	140.6	18.4	80.3	1.06	27	3	2.89
S4-5*	UCS	124-132	1.26	0.52	143.2	19.1	79.6	1.02	33	4	2.72
S4-5	CSC	132-141	1.35	0.67	102.9	25.3	73.0	5.36	33	4	2.63
S4-6	UWC	147-156	1.82	1.38	31.7	52.2	45.6	8.03	N/A	N/A	2.65
S5-3*	UCS	64-72	1.05	0.27	295.9	14.4	84.5	0.46	27	3	1.84

* Indicates the specimens were also tested for UWC.

Table 2. Summary of the creep characteristics for the six permafrost samples.

Sample No.	Temperature (°C)	σ_1 (kPa)	$\dot{\epsilon}_m$ (hr^{-1})	ε_f (%)	θ_s (%)	n	A (hr^{-1} kPa^{-n})	R^2
		103	2.0×10^{-5}					
S4-2	-2	207	1.6×10^{-4}	7.0	20.1	3.31	4.03E-12	0.996
		276	5.4×10^{-4}					
		586	4.2×10^{-6}					
S4-2	-10	793	1.4×10^{-5}	1.3	25.9	5.76	3.97E-22	0.974
		1103	1.6×10^{-4}					
		103	7.0×10^{-6}					
S4-3	-2	172	4.5×10^{-5}	2.5	26.8	4.06	4.36E-14	0.994
		276	3.8×10^{-4}					
		586	3.0×10^{-5}					
S4-3	-10	793	7.2×10^{-5}	2.7	13.9	3.79	8.60E-16	0.983
		1103	3.3×10^{-4}					
		103	3.9×10^{-5}					
S4-4	-2	172	1.3×10^{-4}	4.7	18.4	2.70	1.32E-10	0.991
		276	5.6×10^{-4}					
		586	2.5×10^{-5}					
S4-5	-10	793	1.0×10^{-4}	2.7	25.3	5.38	2.92E-20	0.996
		1103	7.4×10^{-4}					

Note: Samples with the same sample number tested at different temperatures represent different portions of a core segment and, thus, correspond to different samples.

Table 3. Long-term strength estimates for the six permafrost samples.

Sample No.	Temperature (°C)	θ_s (%)	σ_{lt} (kPa)	
			Approach 1	Approach 2
S4-2	-2	20.1	24.5	26.5
S4-2	-10	25.9	257.3	359.4
S4-3	-2	26.8	32.0	44.2
S4-3	-10	13.9	117.9	163.0
S4-4	-2	18.4	12.0	15.3
S4-5	-10	25.3	195.4	245.0

Table 4. Unfrozen gravimetric water content of the tested samples at different temperatures.

Temperature (°C)	S2-4	S2-5	S3-3	S3-5	S3-6	S3-7	S4-2	S4-3	S4-3	S4-5	S4-6	S5-3
-20.02	4.3	3.3	3.1	2.1	2.0	2.3	5.4	1.3	1.4	1.6	1.5	12.1
-10.02	6.1	5.8	3.9	2.6	2.5	3.6	5.9	2.4	1.3	3.1	2.4	12.1
-5.01	9.2	9.3	5.4	3.7	4.1	6.7	8.1	3.2	3.0	6.5	3.8	14.6
-3.03	13.6	13.4	5.9	4.8	5.2	8.4	8.5	4.2	4.2	7.9	5.3	19.3
-2.01	18.3	19.3	6.9	5.7	6.7	11.1	9.5	5.1	4	10.9	7.3	19.9
-1.05	35	37.9	9.1	9.5	11.9	17.3	11.9	6.6	6.5	14.6	13.8	24.9
-0.54	54.8	53.8	13.1	14.2	18.2	25.4	15	9.9	11	20.4	19.9	27.7
+9.98	75.1	80.9	66.7	51.8	67.9	105.7	185.6	83.3	83.6	147.1	26.1	525.7

Figure_1

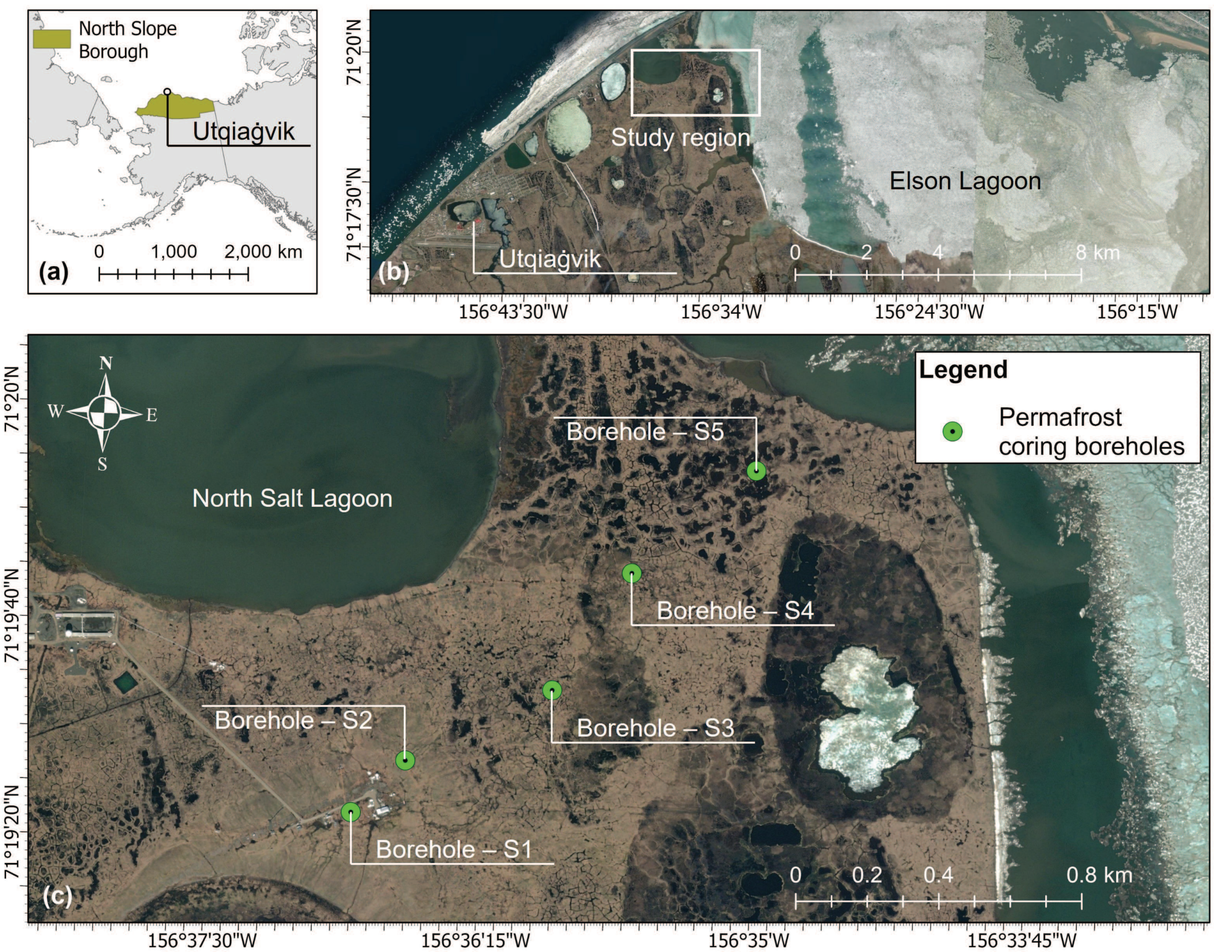
North Slope Borough
Utqiaġvik
0 1,000 2,000 km
(a)
71°20'N
71°17'30"N
Study region
Elson Lagoon
Utqiaġvik
0 2 4 8 km
(b)
156°43'30"W
156°34'W
156°24'30"W
156°15'W
71°20'N
71°19'40"N
71°19'20"N
N
W
E
S
Legend
Permafrost coring boreholes
Borehole – S5
North Salt Lagoon
Borehole – S4
Borehole – S3
Borehole – S2
Borehole – S1
0 0.2 0.4 0.8 km
(c)
156°37'30"W
156°36'15"W
156°35'W
156°33'45"W

Figure_2

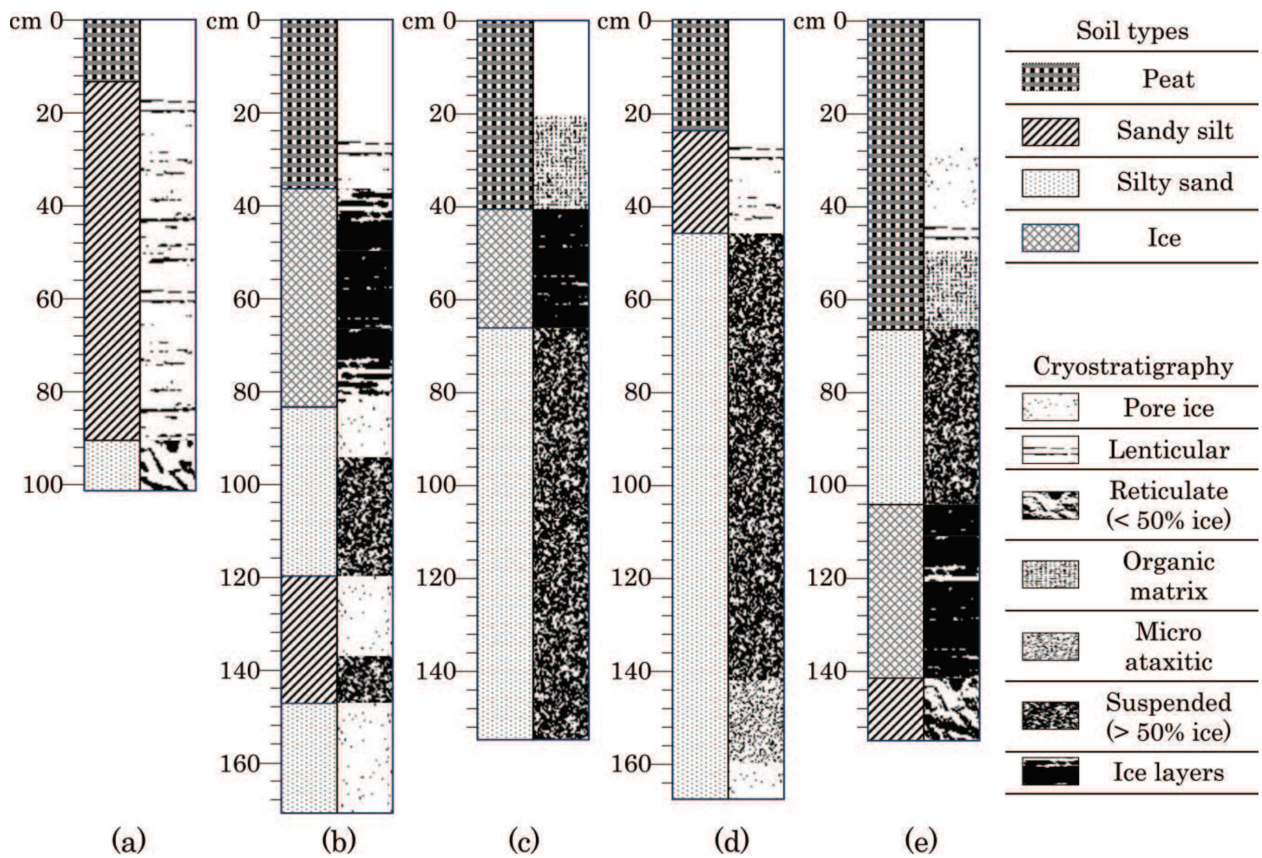

cm 0
20
40
60
80
100
120
140
160
(a)
(b)
(c)
(d)
(e)
Soil types
Peat
Sandy silt
Silty sand
Ice
Cryostratigraphy
Pore ice
Lenticular
Reticulate (< 50% ice)
Organic matrix
Micro ataxitic
Suspended (> 50% ice)
Ice layers

Figure_3

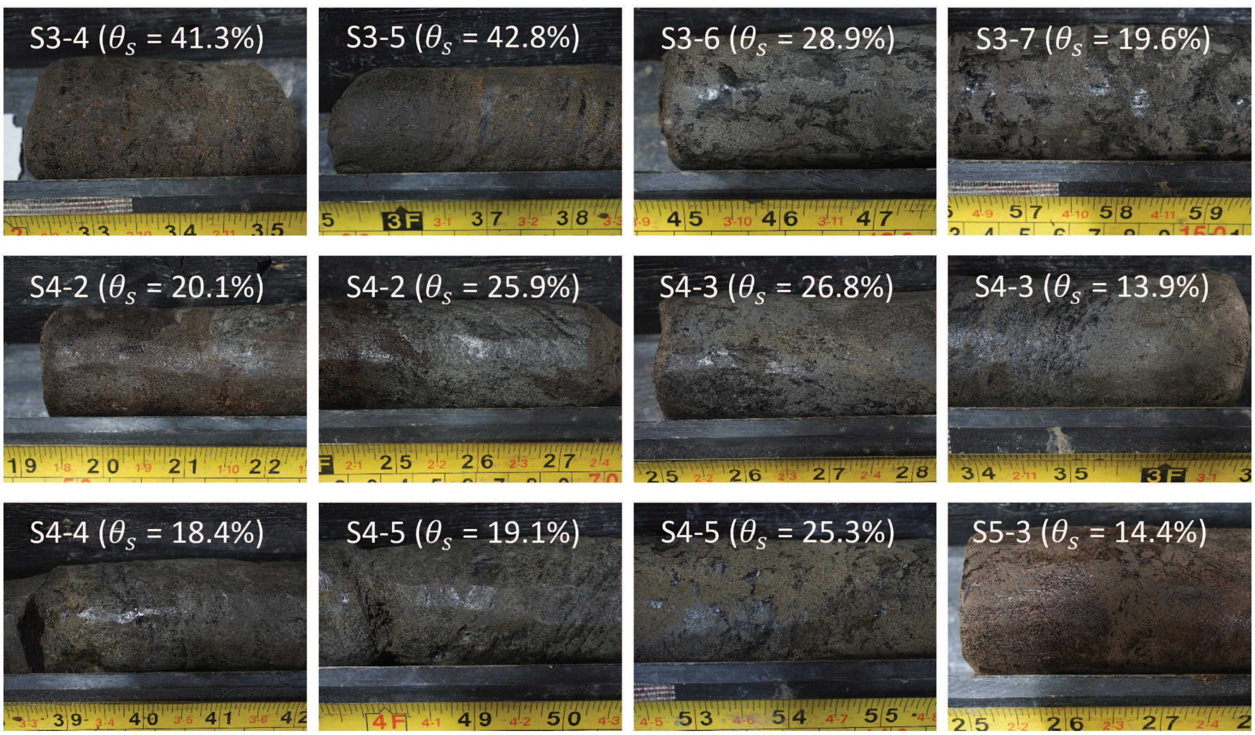

S3-4 (θ_s = 41.3%)
S3-5 (θ_s = 42.8%)
S3-6 (θ_s = 28.9%)
S3-7 (θ_s = 19.6%)
S4-2 (θ_s = 20.1%)
S4-2 (θ_s = 25.9%)
S4-3 (θ_s = 26.8%)
S4-3 (θ_s = 13.9%)
S4-4 (θ_s = 18.4%)
S4-5 (θ_s = 19.1%)
S4-5 (θ_s = 25.3%)
S5-3 (θ_s = 14.4%)

Figure_4

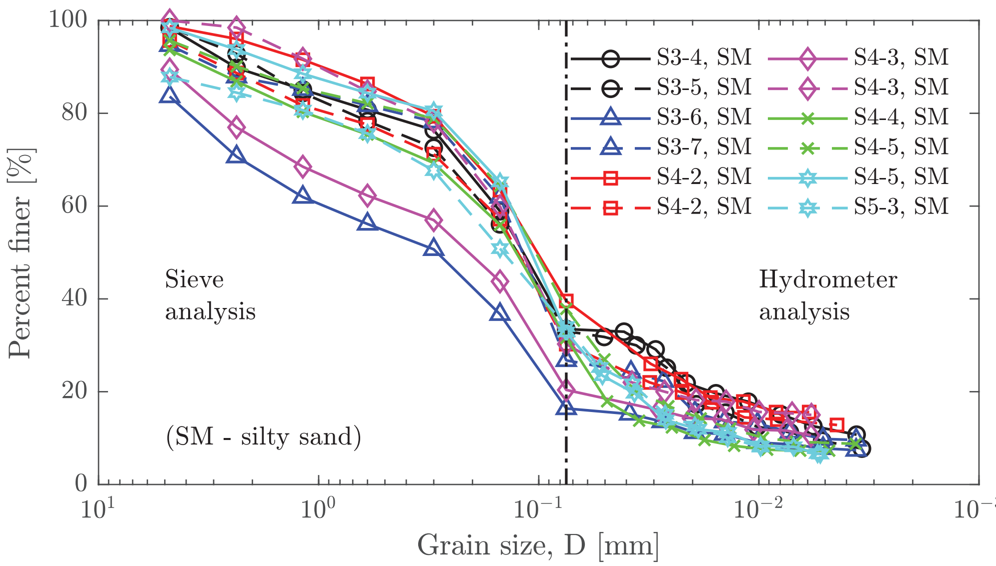

100
80
60
40
20
0
Percent finer [%]
10^1
10^0
10^{-1}
10^{-2}
10^{-3}
Grain size, D [mm]
Sieve analysis
Hydrometer analysis
(SM - silty sand)
S3-4, SM
S3-5, SM
S3-6, SM
S3-7, SM
S4-2, SM
S4-2, SM
S4-3, SM
S4-3, SM
S4-4, SM
S4-5, SM
S4-5, SM
S5-3, SM

Figure_5

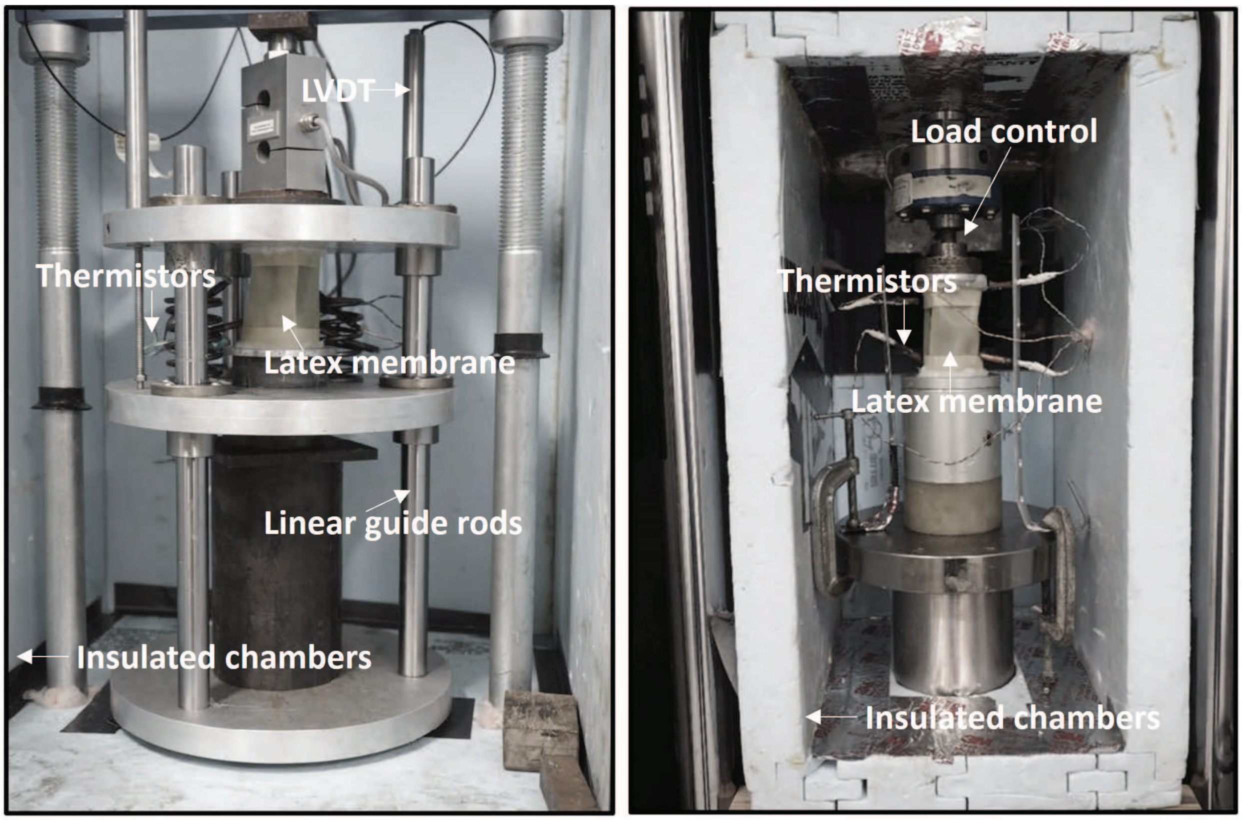

LVDT
Thermistors
Latex membrane
Linear guide rods
Insulated chambers
Load control
Thermistors
Latex membrane
Insulated chambers

(a) (b)

Figure_6

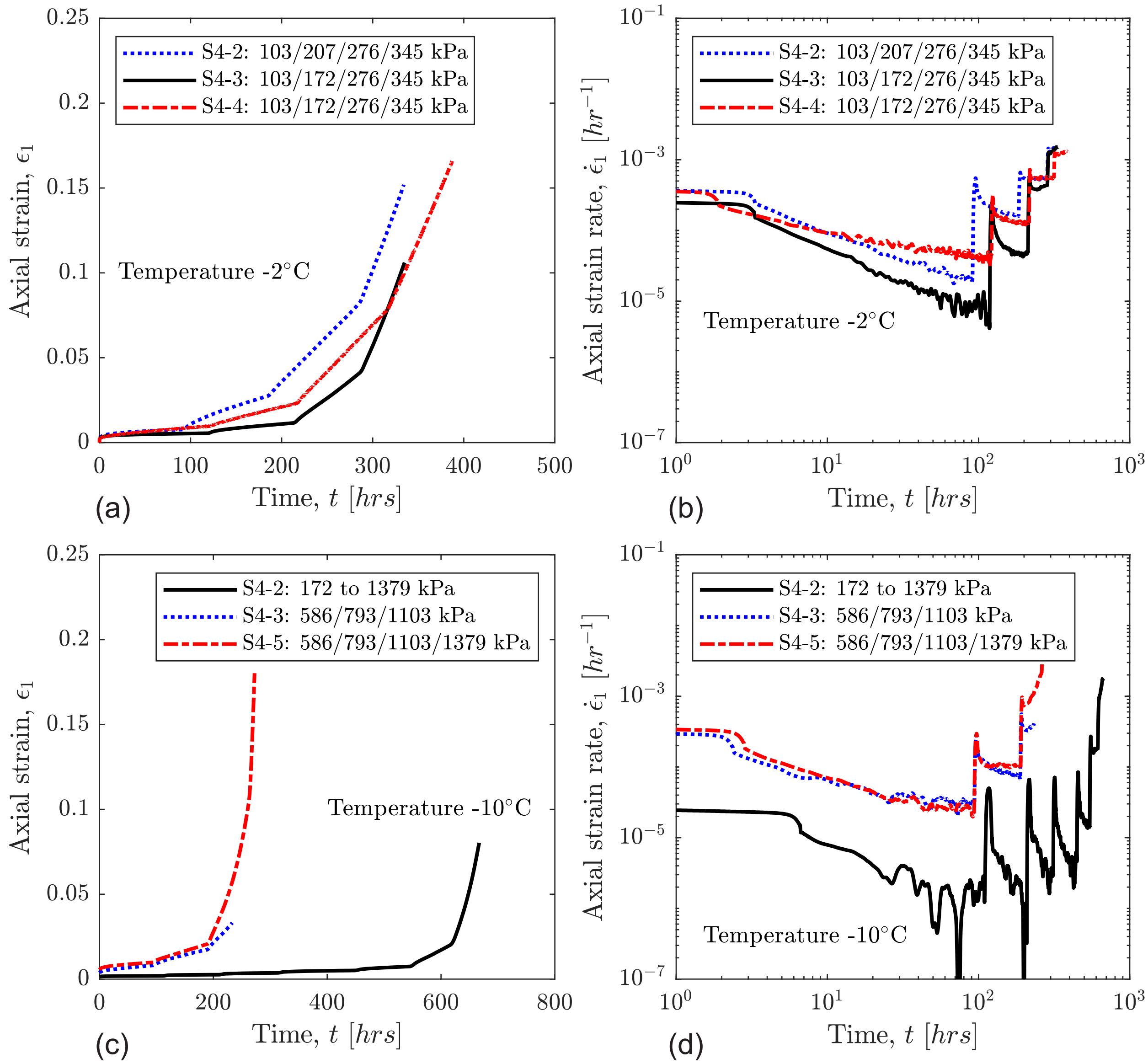

S4-2: 103/207/276/345 kPa
S4-3: 103/172/276/345 kPa
S4-4: 103/172/276/345 kPa
Temperature -2°C
Axial strain, ϵ_1
Time, t $[hrs]$
(a)
Axial strain rate, $\dot{\epsilon}_1$ $[hr^{-1}]$
(b)
S4-2: 172 to 1379 kPa
S4-3: 586/793/1103 kPa
S4-5: 586/793/1103/1379 kPa
Temperature -10°C
(c)
(d)

Figure_7

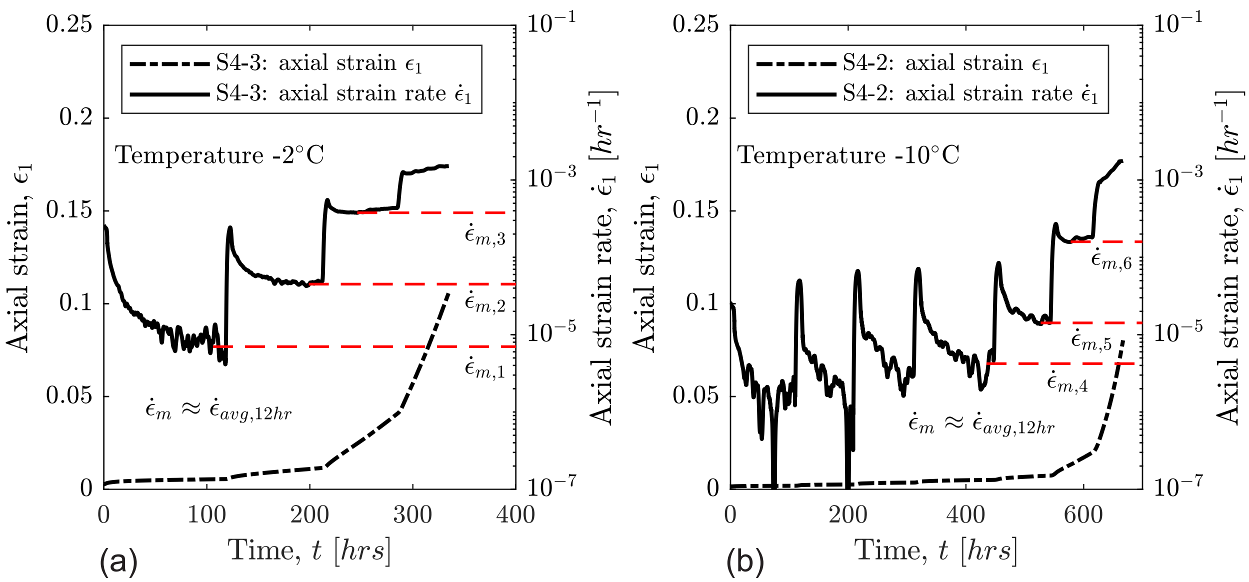

S4-3: axial strain ϵ_1
S4-3: axial strain rate $\dot{\epsilon}_1$
Temperature -2°C
$\dot{\epsilon}_{m,3}$
$\dot{\epsilon}_{m,2}$
$\dot{\epsilon}_{m,1}$
$\dot{\epsilon}_m \approx \dot{\epsilon}_{avg,12hr}$
Axial strain, ϵ_1
Axial strain rate, $\dot{\epsilon}_1$ $[hr^{-1}]$
Time, t $[hrs]$
(a)
S4-2: axial strain ϵ_1
S4-2: axial strain rate $\dot{\epsilon}_1$
Temperature -10°C
$\dot{\epsilon}_{m,6}$
$\dot{\epsilon}_{m,5}$
$\dot{\epsilon}_{m,4}$
$\dot{\epsilon}_m \approx \dot{\epsilon}_{avg,12hr}$
Axial strain, ϵ_1
Axial strain rate, $\dot{\epsilon}_1$ $[hr^{-1}]$
Time, t $[hrs]$
(b)

Figure_8

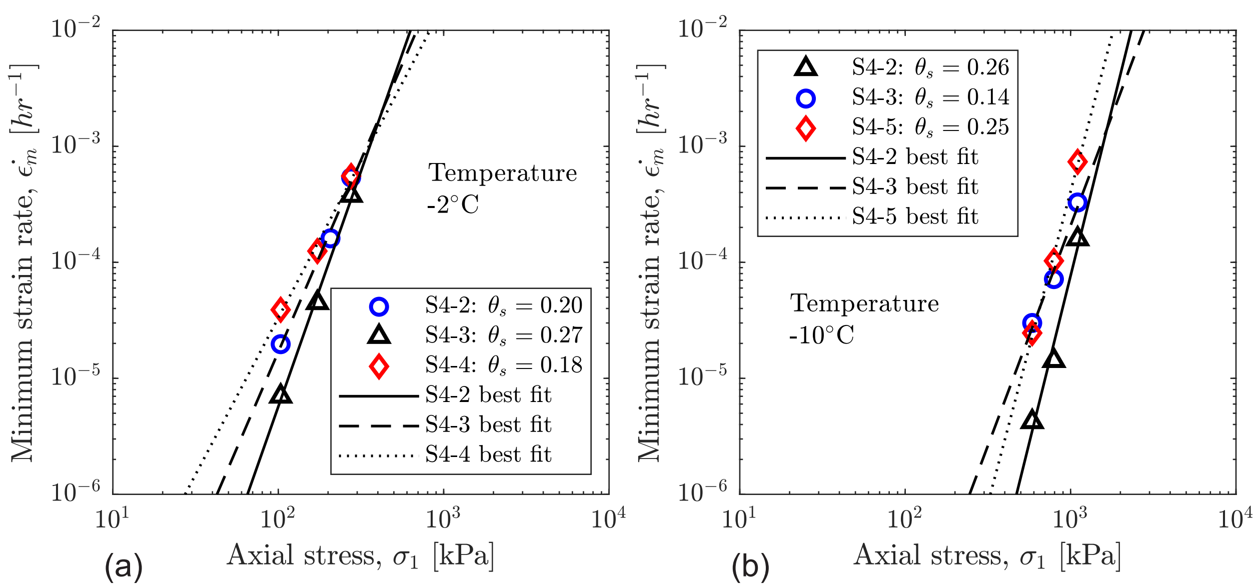

Minimum strain rate, $\dot{\epsilon}_m$ $[hr^{-1}]$
Temperature
-2°C
S4-2: $\theta_s = 0.20$
S4-3: $\theta_s = 0.27$
S4-4: $\theta_s = 0.18$
S4-2 best fit
S4-3 best fit
S4-4 best fit
Axial stress, σ_1 [kPa]
(a)
Minimum strain rate, $\dot{\epsilon}_m$ $[hr^{-1}]$
S4-2: $\theta_s = 0.26$
S4-3: $\theta_s = 0.14$
S4-5: $\theta_s = 0.25$
S4-2 best fit
S4-3 best fit
S4-5 best fit
Temperature
-10°C
Axial stress, σ_1 [kPa]
(b)

Figure_9

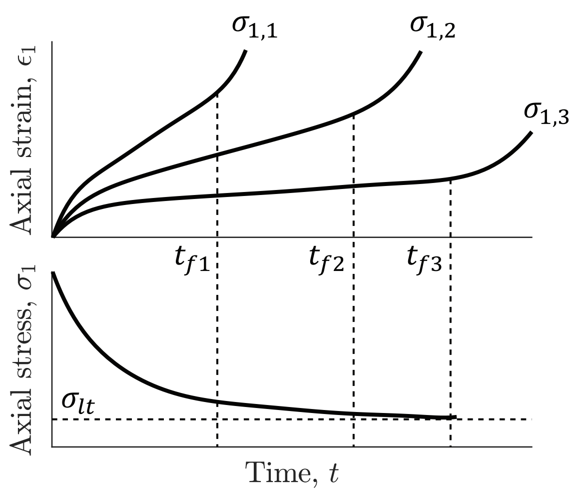

$\sigma_{1,1}$
$\sigma_{1,2}$
$\sigma_{1,3}$
Axial strain, ϵ_1
t_{f1}
t_{f2}
t_{f3}
Axial stress, σ_1
σ_{lt}
Time, t

Figure_10

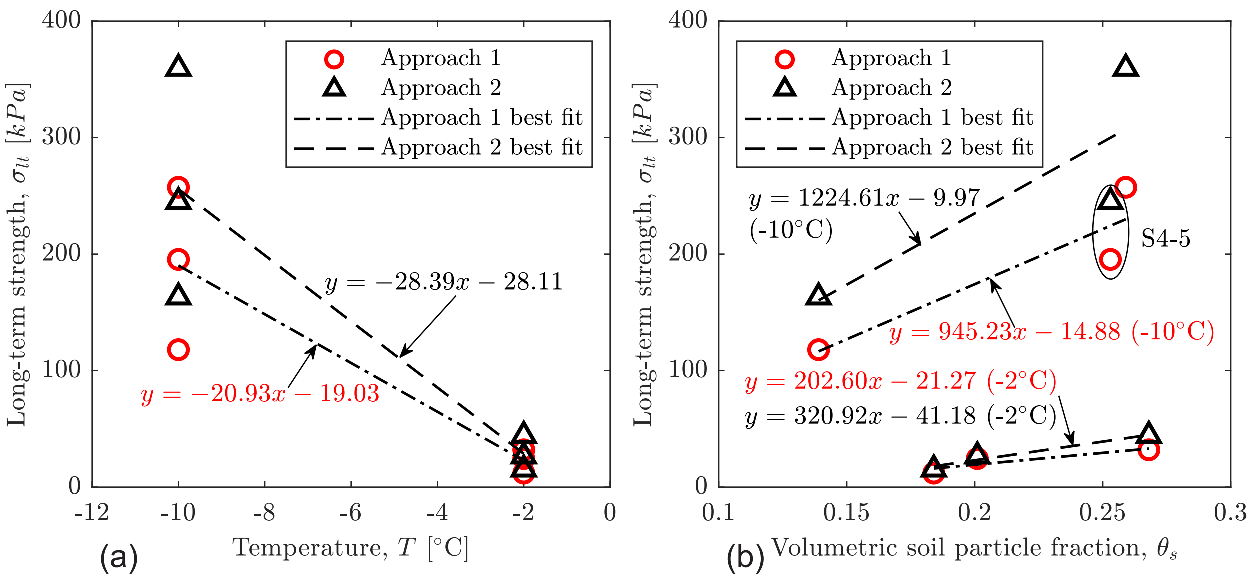

400
300
200
100
0
-12
-10
-8
-6
-4
-2
0
Long-term strength, σ_{lt} $[kPa]$
Temperature, T [°C]
Approach 1
Approach 2
Approach 1 best fit
Approach 2 best fit
$y = -28.39x - 28.11$
$y = -20.93x - 19.03$
(a)
0.1
0.15
0.2
0.25
0.3
Volumetric soil particle fraction, θ_s
$y = 1224.61x - 9.97$
(-10°C)
S4-5
$y = 945.23x - 14.88$ (-10°C)
$y = 202.60x - 21.27$ (-2°C)
$y = 320.92x - 41.18$ (-2°C)
(b)

Figure_11

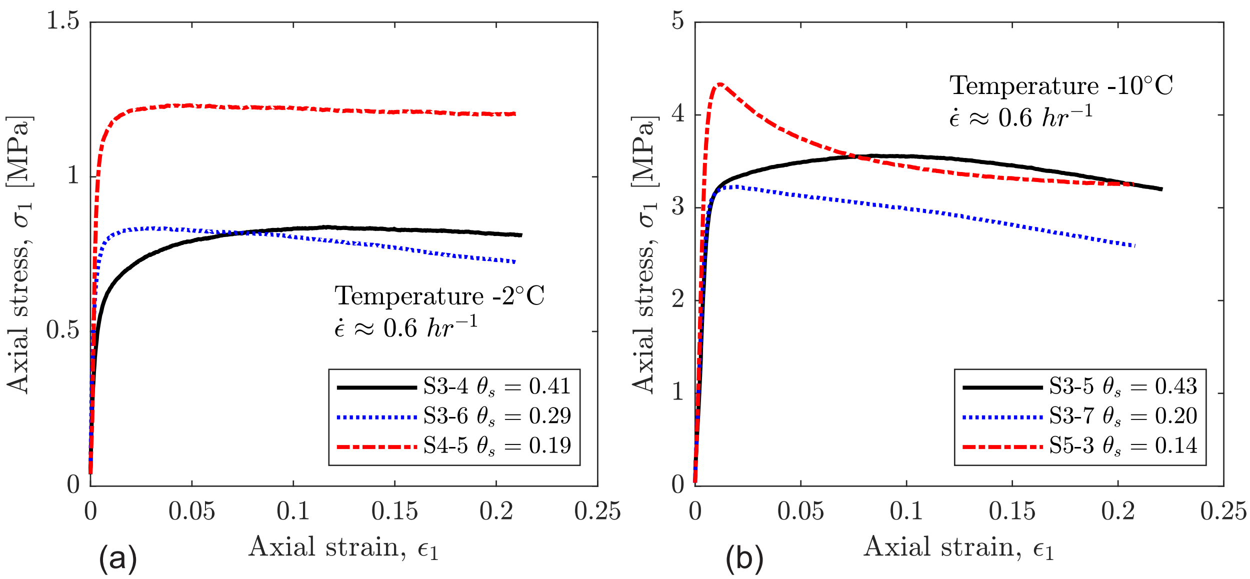

1.5
1
0.5
0
Axial stress, σ_1 [MPa]
0
0.05
0.1
0.15
0.2
0.25
Axial strain, ϵ_1
Temperature -2°C
$\dot{\epsilon} \approx 0.6\ hr^{-1}$
S3-4 $\theta_s = 0.41$
S3-6 $\theta_s = 0.29$
S4-5 $\theta_s = 0.19$
(a)
5
4
3
2
1
0
Axial stress, σ_1 [MPa]
0
0.05
0.1
0.15
0.2
0.25
Axial strain, ϵ_1
Temperature -10°C
$\dot{\epsilon} \approx 0.6\ hr^{-1}$
S3-5 $\theta_s = 0.43$
S3-7 $\theta_s = 0.20$
S5-3 $\theta_s = 0.14$
(b)

Figure_12

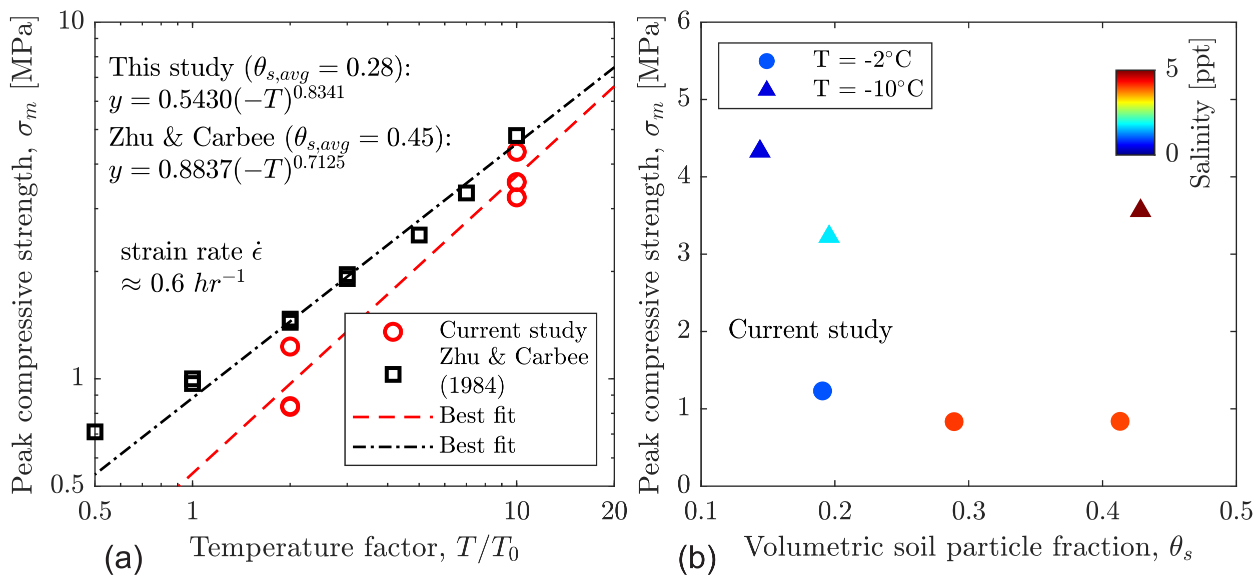

This study ($\theta_{s,avg} = 0.28$):
$y = 0.5430(-T)^{0.8341}$
Zhu & Carbee ($\theta_{s,avg} = 0.45$):
$y = 0.8837(-T)^{0.7125}$
strain rate $\dot{\epsilon}$
$\approx 0.6\ hr^{-1}$
Current study
Zhu & Carbee (1984)
Best fit
Best fit
Peak compressive strength, σ_m [MPa]
Temperature factor, T/T_0
(a)
T = -2°C
T = -10°C
Salinity [ppt]
Current study
Volumetric soil particle fraction, θ_s
(b)

Figure_13

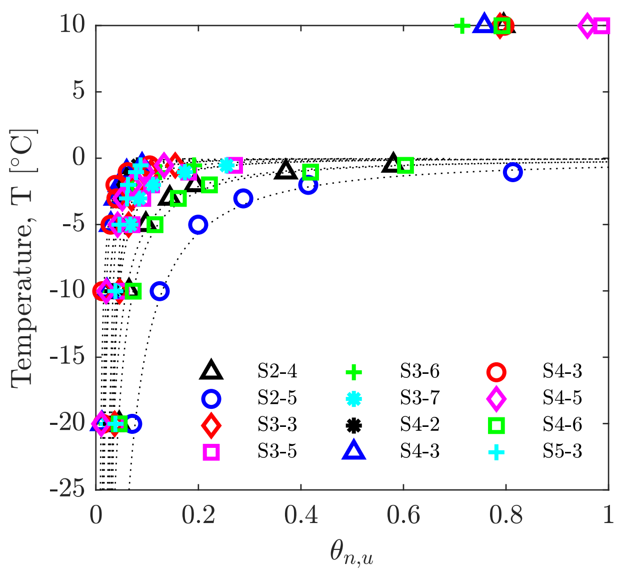

10
5
0
-5
-10
-15
-20
-25
Temperature, T [°C]
0
0.2
0.4
0.6
0.8
1
$\theta_{n,u}$
S2-4
S2-5
S3-3
S3-5
S3-6
S3-7
S4-2
S4-3
S4-3
S4-5
S4-6
S5-3

Figure_14

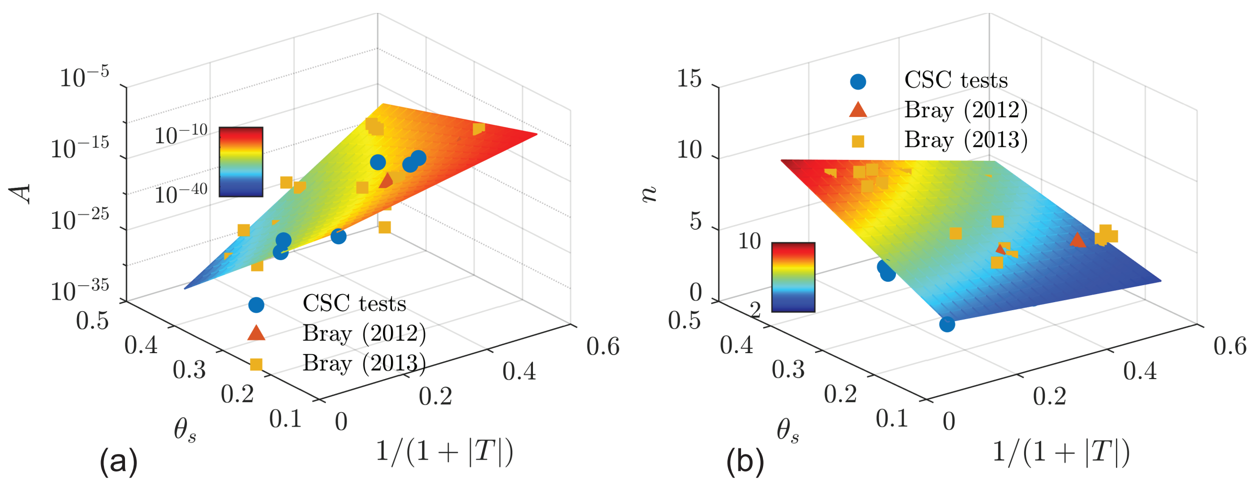

10^{-5}
10^{-15}
10^{-25}
10^{-35}
A
10^{-10}
10^{-40}
CSC tests
Bray (2012)
Bray (2013)
0.5
0.4
0.3
0.2
0.1
θ_s
0
0.2
0.4
0.6
$1/(1+|T|)$
(a)
15
10
5
0
n
10
2
CSC tests
Bray (2012)
Bray (2013)
0.5
0.4
0.3
0.2
0.1
θ_s
0
0.2
0.4
0.6
$1/(1+|T|)$
(b)

Figure_15

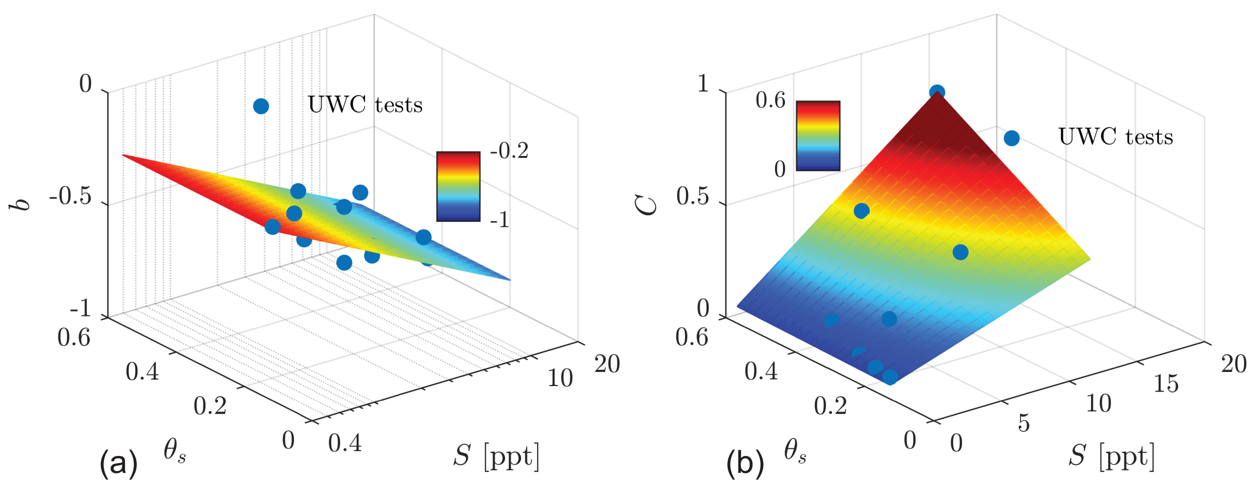

UWC tests
-0.2
-1
0
-0.5
-1
b
0.6
0.4
0.2
0
θs
0.4
10
20
S [ppt]
(a)
1
0.5
0
C
0.6
0
UWC tests
0.6
0.4
0.2
0
θs
0
5
10
15
20
S [ppt]
(b)

Figure_16

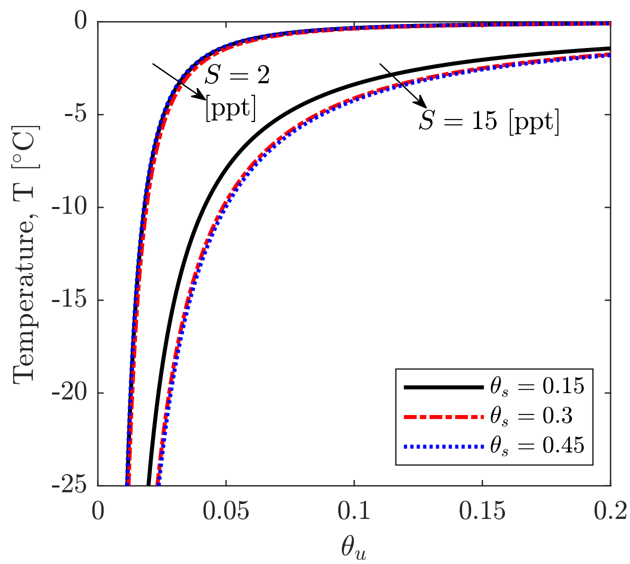

0
-5
-10
-15
-20
-25
Temperature, T [°C]
0
0.05
0.1
0.15
0.2
θ_u
$S = 2$ [ppt]
$S = 15$ [ppt]
$\theta_s = 0.15$
$\theta_s = 0.3$
$\theta_s = 0.45$

Figure_17

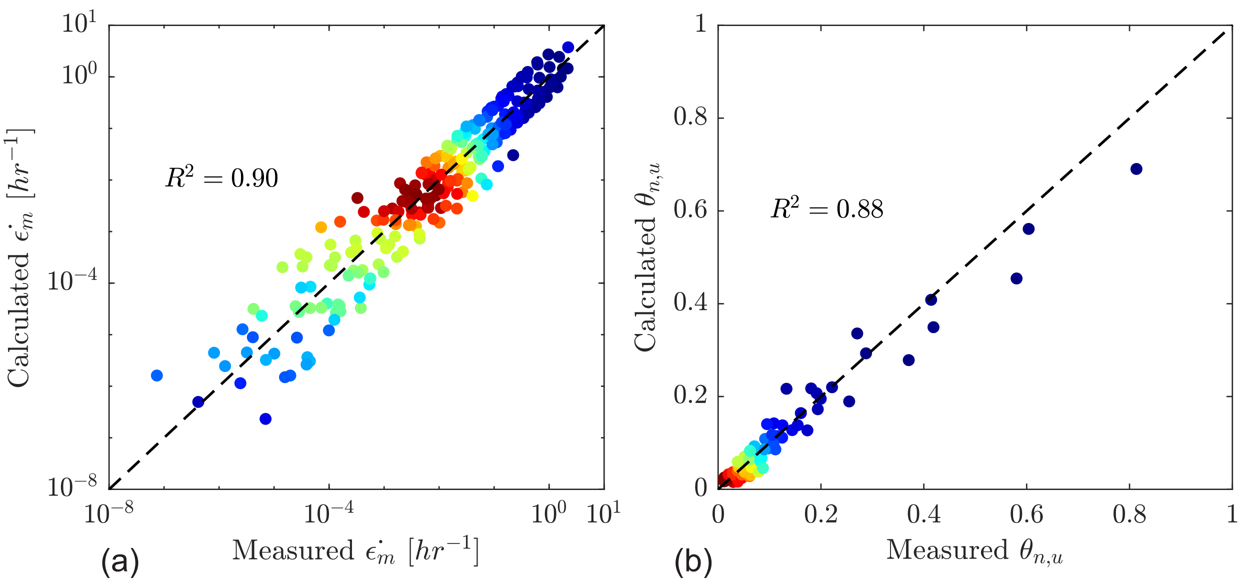

$R^2 = 0.90$
Calculated $\dot{\epsilon_m}$ $[hr^{-1}]$
Measured $\dot{\epsilon_m}$ $[hr^{-1}]$
10^{1}
10^{0}
10^{-4}
10^{-8}
(a)
$R^2 = 0.88$
Calculated $\theta_{n,u}$
Measured $\theta_{n,u}$
0
0.2
0.4
0.6
0.8
1
(b)

Figure_18

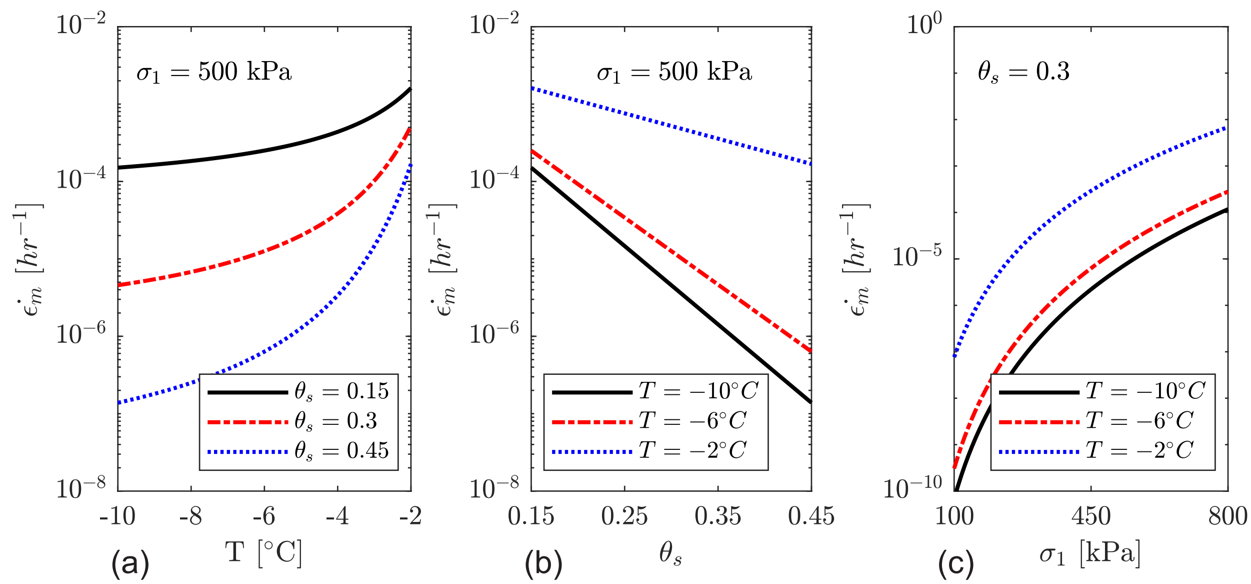

$\sigma_1 = 500$ kPa
$\theta_s = 0.15$
$\theta_s = 0.3$
$\theta_s = 0.45$
$\dot{\epsilon}_m$ $[hr^{-1}]$
T [°C]
(a)
$\sigma_1 = 500$ kPa
$T = -10°C$
$T = -6°C$
$T = -2°C$
θ_s
(b)
$\theta_s = 0.3$
$T = -10°C$
$T = -6°C$
$T = -2°C$
σ_1 [kPa]
(c)

Figure_19

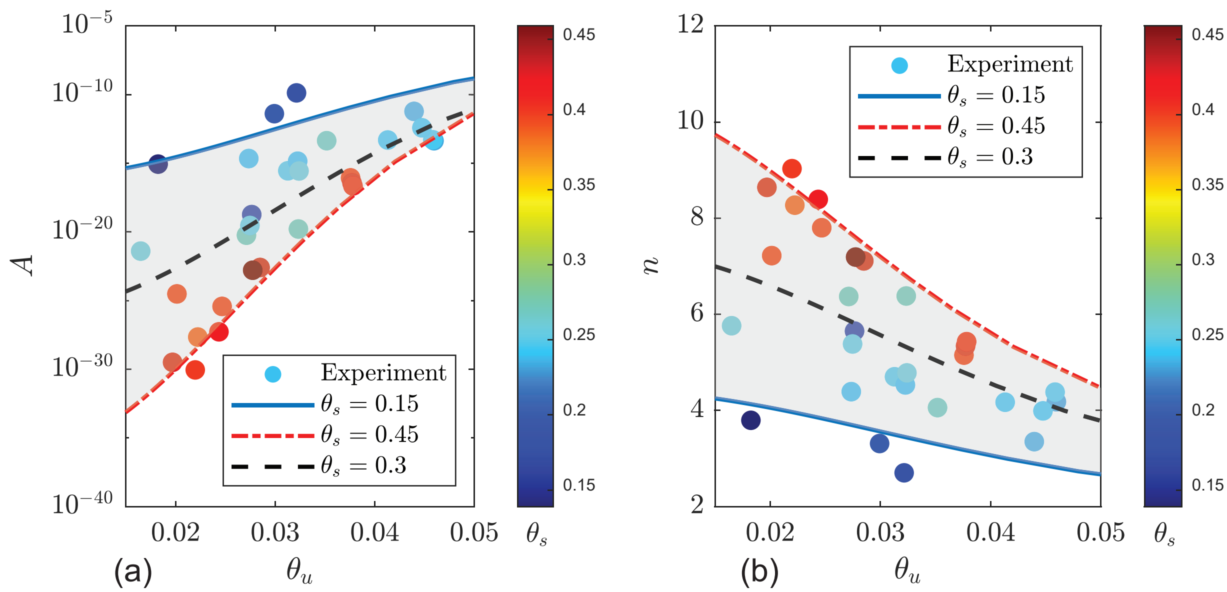

(a)
A
θ_u
θ_s
Experiment
$\theta_s = 0.15$
$\theta_s = 0.45$
$\theta_s = 0.3$
(b)
n
θ_u
θ_s
Experiment
$\theta_s = 0.15$
$\theta_s = 0.45$
$\theta_s = 0.3$

Figure_20

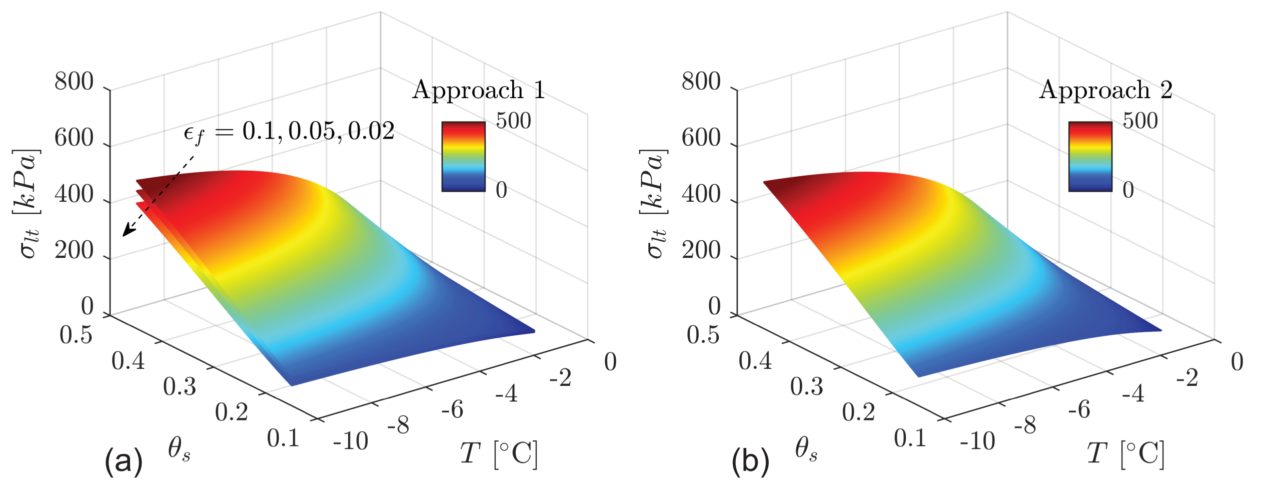

Approach 1
500
0
$\epsilon_f = 0.1, 0.05, 0.02$
800
600
400
200
0
σ_{lt} $[kPa]$
0.5
0.4
0.3
0.2
0.1
θ_s
-10
-8
-6
-4
-2
0
T [°C]
(a)
Approach 2
500
0
800
600
400
200
0
σ_{lt} $[kPa]$
0.5
0.4
0.3
0.2
0.1
θ_s
-10
-8
-6
-4
-2
0
T [°C]
(b)

Figure_21

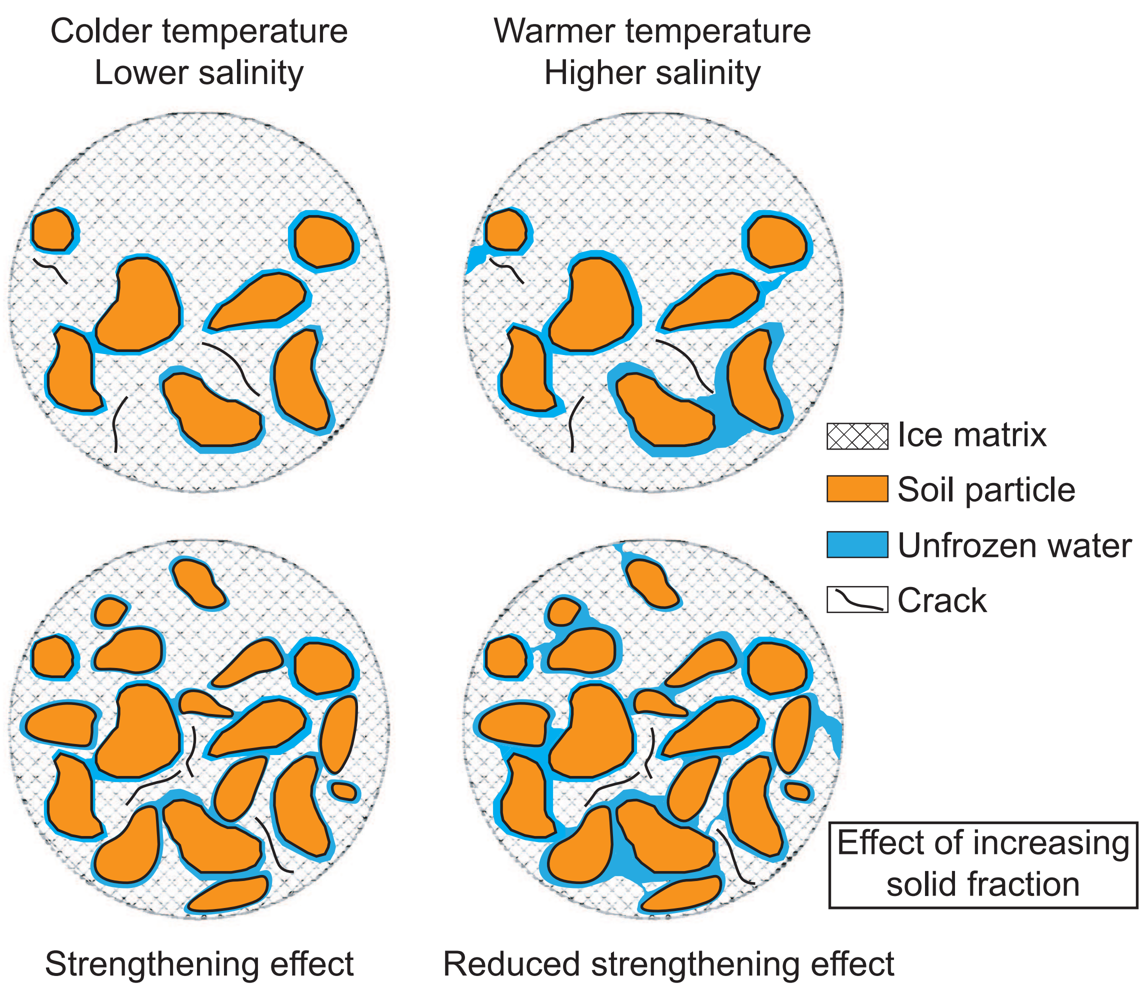
Colder temperature
Lower salinity
Warmer temperature
Higher salinity
Ice matrix
Soil particle
Unfrozen water
Crack
Effect of increasing solid fraction
Strengthening effect
Reduced strengthening effect

Figure_22

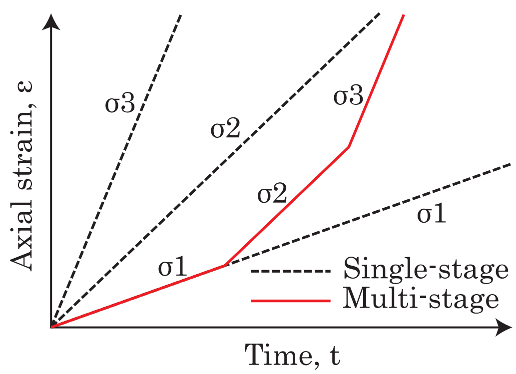
Axial strain, ε
σ3
σ2
σ3
σ2
σ1
σ1
Single-stage
Multi-stage
Time, t